

CHAPTER 7

TRACE WATER VAPOR ANALYSIS IN SPECIALTY GASES: SENSOR AND SPECTROSCOPIC APPROACHES

MARK W. RAYNOR,¹ KRIS A. BERTNESS,² KEVIN C. COSSEL,³ FLORIAN ADLER,³ AND JUN YE³

¹Matheson, Advanced Technology Center, Longmont, Colorado

²National Institute of Standards and Technology, Boulder, Colorado

³JILA, National Institute of Standards and Technology, and University of Colorado, Department of Physics, Boulder, Colorado

7.1 Introduction

The analysis of water vapor impurity (often also referred to as *moisture*) is important in a number of specialty gas applications. However, the main driver for the development and advancement of trace moisture analysis techniques has been the microelectronics industry. The International Technology Roadmap for Semiconductors (ITRS) details the gas purity requirements for various wafer fabrication processes on their website (www.itrs.net). Oxygenated contaminants such as water vapor in the materials used and in the wafer environment are primary causes of defects and process variations that compromise yield. Because even trace levels of water in the process gases can seriously decrease device performance, analytical techniques must be capable of detecting water vapor from ppmv ($\mu\text{mol/mol}$) down to the low and even sub-ppbv (nmol/mol) range.

Measurement of water vapor at trace levels is quite challenging not only due to the adsorptive nature of the water molecule on metal and other surfaces, but also because of the range of gas matrices (including inert, oxide, halide, hydride, corrosive, hy-

drocarbon, and halocarbon gases) that can potentially interfere with the measurement process. There is no single approach that meets all analysis requirements, and hence a range of techniques have been investigated over the years [1]. These include:

- (a) Gas chromatography (GC)
- (b) Mass spectrometry with electron impact and atmospheric pressure ionization sources (EI-MS, APIMS)
- (c) Ion mobility spectrometry (IMS)
- (d) Sensor-based methods such as chilled-mirror hygrometry, oscillating quartz crystal microbalance (QCM), capacitance cell, and electrolytic cell
- (e) Spectroscopic methods such as Fourier transform infrared (FTIR) spectroscopy, tunable diode laser absorption spectroscopy (TDLAS), cavity ring-down spectroscopy (CRDS), intracavity laser spectroscopy (ILS), and cavity-enhanced frequency-comb spectroscopy (CE-DFCS)

Some approaches are better suited than others to water vapor analysis. For example, gas chromatography and mass spectrometry, methods that are more commonly used for analyzing other gas-phase impurities, are not employed routinely for quantitative water vapor measurements in many specialty gases. This is due mainly to issues such as elevated water vapor background concentrations in the instrumentation, loss of water vapor due to adsorption, sampling difficulties, matrix gas interference, poor sensitivity, or need for frequent calibration. Reaction GC, where, by reaction with calcium carbide, water in the sample is converted to acetylene, a species that is easier to chromatograph, is an option for ppmv-level water vapor detection. However, a reported variance of ± 1 ppmv for water vapor challenges in helium and ammonia precludes its use for sub-ppmv analysis [2]. Mass spectrometry-based methods can be used but suffer from water vapor background and drift issues. Further, the sensitivity of electron impact ionization sources is limited to around 0.5 ppmv water vapor levels unless selected matrix gases such as helium or hydrogen are used [1]. Atmospheric pressure ionization mass spectrometry (discussed in more detail in Chapter 5) and ion mobility spectrometry offer sub-ppbv detection capability for water vapor in bulk gases and are employed primarily for gases such as argon, nitrogen, helium, and hydrogen [3–6]. However, neither of these techniques is commonly applied in specialty gases. In many cases the high ionization potential of water prevents ionization by charge transfer. Therefore, APIMS methods in gases such as ammonia, silane, germane, and hydrogen chloride require development of specialized ionization mechanisms and cluster analysis by specialized personnel in order to measure water vapor [7–10]. Further, corrosion of source components, formation of solid decomposition products, and the potential for contamination also complicate analysis of many reactive hydride and corrosive gases.

In this chapter we therefore focus on technologies that not only provide high sensitivity for water vapor but can also be applied to a wide range of specialty gases. They can be broadly categorized into sensor- and spectroscopic-based approaches. Aspects related to water standards and calibration are also discussed.

7.2 Primary Standards for Water Vapor Measurement

The primary standard for water vapor measurement in gases is the standard hygrometer, which has been developed to achieve an expanded uncertainty of 0.1 % for water vapor in inert gases at concentrations of 250 $\mu\text{g/g}$ or above. (The expanded uncertainty, u , is defined as the range that covers two standard deviations, σ , about the mean of a normal distribution of measurements $u = k\sigma$ with $k = 2$, for a 95 % confidence interval.) The standard hygrometer maintained at the National Institute of Standards and Technology (NIST) has recently been improved to achieve this level and also to measure lower concentrations (down to 250 $\mu\text{g/g}$) with somewhat higher uncertainty (1 %) [11]. This hygrometer measures water vapor by separating it from the carrier gas using desiccant material and cold traps and then measuring both the change in weight of the traps and the total mass of dried carrier gas that flowed during the sampling period. The centerpiece of this instrument is a set of prover tubes that collect the dry gas and measure its volume, temperature, and pressure with high accuracy (see Figure 7.1). The ideal gas law is then applied to calculate the total mass of the gas collected. A complete description of the system and uncertainty analysis is given by Meyer et al. [11].

Although the NIST standard gravimetric hygrometer can achieve exceptional accuracy, as with many primary standards, its design emphasizes accuracy over convenience. The system is not readily transportable and requires long measurement periods and control of ambient conditions to maintain accuracy. Transfer of the measurement to secondary methods is accomplished by using the standard hygrometer to characterize primary humidity generators, which are then used to calibrate hygrometers for field use, such as chilled-mirror hygrometers, electrolytic hygrometers, and cavity ring-down spectroscopy systems. NIST maintains two such primary humidity generators, the hybrid humidity generator (HHG) [12] and the low-frost-point generator (LFPG) [13], as a part of their calibration services for portable hygrometers. Both of these systems generate saturated water vapor in equilibrium with a carrier gas (typically, purified air or nitrogen) at a constant temperature. The concentration of water vapor at the system outlet can be varied either by adjusting the gas pressure after leaving the saturation chamber or by mixing in additional dry gas, or both. The HHG shown in Figure 7.2 has a range of water vapor mole fractions from 1 ppmv to 0.3 % (frost-point/dew-point temperatures from -76 to 40°C). Compared to the NIST standard hygrometer described above, the two systems agreed within their combined expanded ($k = 2$) uncertainty of 0.22 %. As its name suggests, the LFPG was developed to calibrate instrumentation in even lower water vapor concentration ranges, from 3 ppmv down to 3 ppbv, corresponding to frost-point temperatures from -10 to -100°C . Volumetric flow rates of up to 4 slpm can be accommodated. The relative expanded ($k = 2$) uncertainty for low-water-vapor mole fractions (3 nmol/mol) is only 0.8 % [14].

The LFPG also forms the basis of a new transfer calibration standard based on permeation tube humidity generators. These generators flow liquid water through a tube with a stable permeation rate into a gas stream in a temperature-stabilized chamber from which the humidified gas is extracted and then mixed with additional

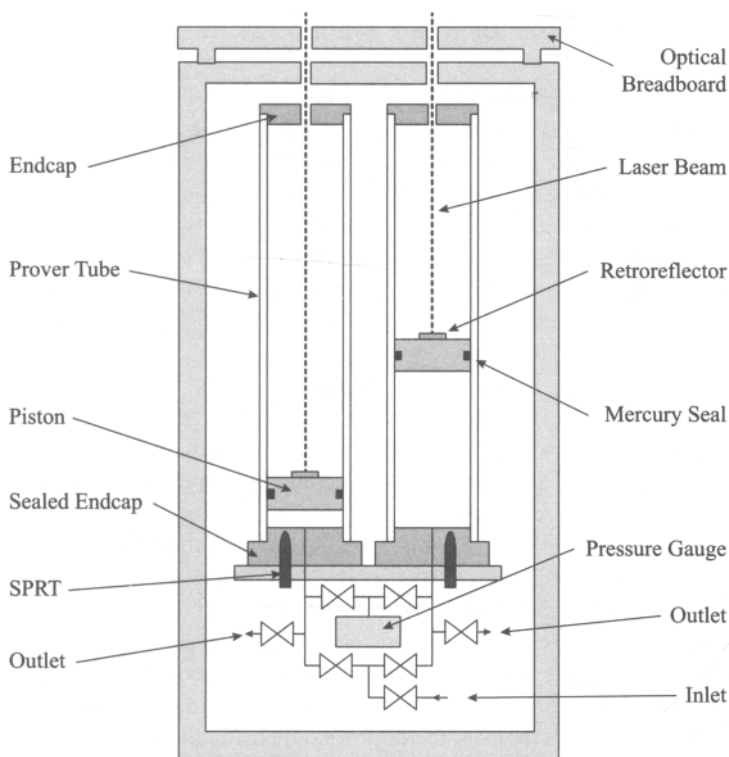


Figure 7.1 Prover tubes from a second-generation NIST standard hygrometer. Each prover tube is about 1 m in length and 14 cm in diameter.

dry gas if desired. The low cost and high stability of these systems makes them popular for the calibration of various commercial detectors. The exact permeation rate of a given tube, however, is difficult to predict from its geometry and average materials properties. Using a nulling technique whereby the humidity output of the primary standard LFPG is set equal to that of a permeation tube generator under test, errors related to humidity analyzer zero, nonlinearity, and absolute response can be eliminated. By use of this technique, the permeation rate of a typical tube was found to be stable to within 7 % over five calibrations spanning a nine-month period, varying less than 1 ppbv over the total gas flow range of the permeation tube generator [15]. This stability compares favorably with 10 to 30 % errors for permeation tube moisture generators calibrated with less reliable methods.

A portable humidity source alternative to a permeation tube is the water diffusion vial. These vials contain a reservoir connected to a long narrow capillary tube that restricts the flow of water vapor. The mass diffusion of water out of the vial depends on the vial temperature, total gas pressure, and capillary cross-sectional area, along with diffusion and density parameters for water vapor. The mass diffusion rate can be calculated within approximately 10 % for a given diffusion vial, or the vial

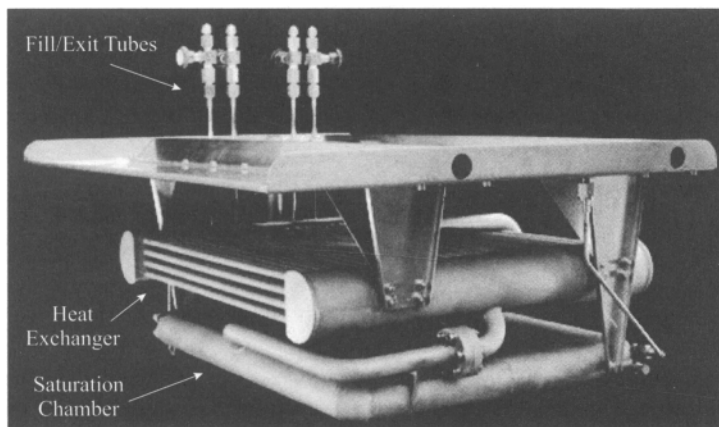


Figure 7.2 Final saturation chamber of a NIST hybrid humidity generator. During actual operation, this portion of the system is submerged in a temperature-controlled bath.

can be maintained at constant pressure and temperature for several days or weeks and its change in mass measured with a precision balance. Mass flow rates of 1×10^{-6} g/min are typical. When the diffusion vial is placed in a stream of dry gas, the water vapor concentration is a simple function of the mass diffusion rate, total pressure, temperature, and carrier gas flow rate.

7.2.1 Sampling for Instrument Calibration and Gas Analysis

A generic manifold for generating and delivering water vapor standards to analytical instrumentation as well as for the analysis of specialty gas samples for water vapor is shown in Figure 7.3. For calibration, known concentrations of water vapor in dry nitrogen are first generated in diffusion or permeation systems as described above and diluted dynamically [16]. This entails spiking the moist stream into a stream of the dried sample matrix gas under set conditions of flow rate, temperature, and pressure to generate standards at different concentrations. Dry matrix gas is typically required as a reference or diluent for most instruments and is obtained by passing the sample gas through a suitable purifier for the gas concerned. Since the water vapor added to the dry matrix gas is in a nitrogen or inert carrier stream, the amount of carrier gas is typically kept below 10 % to minimize any effects of the matrix gas composition on the instrument response. This is particularly important for spectroscopic methods, as discussed later in the chapter.

As water is adsorptive, the surface area and dead-volume regions within the sampling manifold are minimized in the design. This approach ensures that the water vapor concentration rapidly equilibrates in the gas delivered to the analyzer. Regulators, sampling lines, and the analyzer are also thermally controlled (e.g., 60 °C) to hasten equilibration and to prevent ambient temperature fluctuations from affecting the readings. An electronic pressure controller is most often installed downstream of

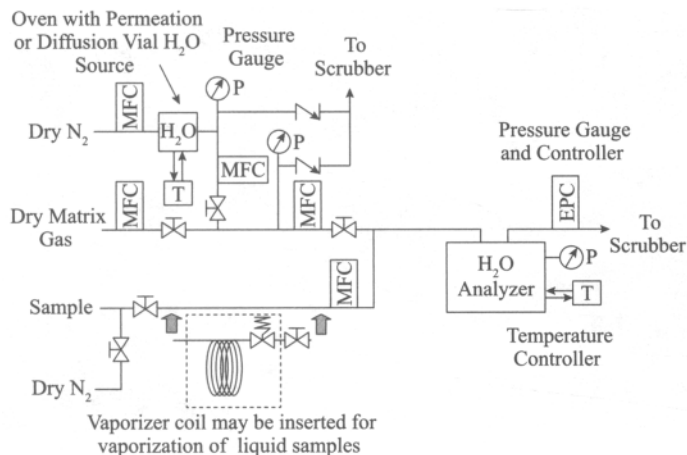


Figure 7.3 Generic manifold for instrument calibration and sample gas analysis.

the measurement point so that pressure can be accurately controlled in the analyzer. Manifold materials require careful selection, as the addition of water vapor/nitrogen to some reactive and acid gases can result in corrosion and particulate generation. Electropolished 316 stainless steel components and lines are most commonly used. However, other alloys, such as Hastelloy, are preferred for corrosive gases such as hydrogen bromide. Additional information, including the effects of reactions between process gases and tubing walls, may be found in the review by Funke et al. [1].

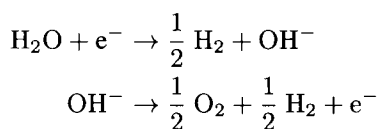
Water vapor in the sample gas is measured by flowing gas from the cylinder directly to the calibrated analyzer. In the case of compressed liquefied gases, liquid-phase sample can also be withdrawn from the cylinder and vaporized in a vaporizer coil prior to introduction to the analyzer (Figure 7.3). In both cases, sample gas is delivered to the analyzer under the same conditions of temperature and pressure as those used for calibration.

7.3 Sensor Technologies

There are a number of conventional sensor technologies used for water vapor detection that rely on adsorption or condensation of water vapor from the gas sample onto solid materials. These are typically robust, convenient, fairly inexpensive devices that have a small footprint and are widely used in inert or nonreactive gas matrices. Four main sensor technologies are discussed here.

7.3.1 Electrolytic Cells

Electrolytic hygrometers operate on the basis that water molecules can be electrolyzed into molecular oxygen and hydrogen by application of a voltage greater than the thermodynamic decomposition voltage of water (2 V). A typical electrolytic hygrometer comprises a sensing cell coated with a thin film of phosphorus pentoxide electrolyte, which is highly hygroscopic and absorbs water from the sample gas stream forming $P_2O_5(H_2O)_n$. The cell consists of a hollow glass tube with two inert platinum or rhodium electrodes spirally wound around the inside wall and in contact with the phosphorus pentoxide electrolyte layer (Figure 7.4). The gas sample flows through the tube at a set flow rate (100 mL/min) and contacts the phosphorus pentoxide electrolyte. By applying an electrical potential to the electrodes, the water in the film is electrolyzed. Once equilibrium is reached, the rate at which water molecules enter the cell will exactly match the rate at which molecules are electrolyzed. Each water molecule produces the flow of two electrons through the external circuit as shown below, and the steady-state current created by these electrons can be related directly to the water concentration using Faraday's law and the sample flow rate.



The theory of operation of phosphorus pentoxide electrolytic hygrometers has been discussed in more detail by McAndrew [17] and Wiederhold [18].

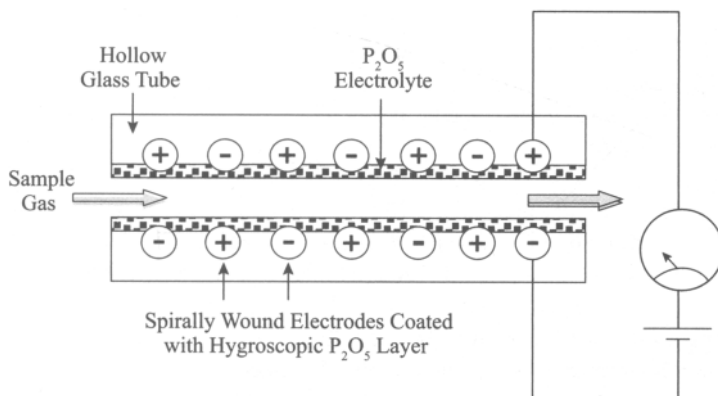


Figure 7.4 P₂O₅ electrolytic sensor.

Phosphorus pentoxide electrolytic cells were invented by Keidel [19] and developed by the DuPont Company. The technology is commercially available today

from companies such as Meeco and GOW-MAC Instruments.* Since phosphorus pentoxide cells are used in the electrolysis of water vapor, the method is often considered to be a primary measurement method. However, cell-specific effects and different modes of operation that result in measurement errors are observed, and therefore certification against a water vapor standard is recommended on a periodic basis. Typical electrolytic hygrometers can detect water vapor in the range from a few ppbv to 2000 ppmv with an accuracy of $\pm 5\%$, provided that the flow rate of the sample gas through the cell is properly controlled. Water vapor levels higher than 2000 ppmv should be avoided, as the electrolyte will become completely hydrated and form liquid orthophosphoric acid that can leave the cell. At low water vapor concentrations, loss in sensitivity and long equilibration and response times can be experienced, especially when the sensor has been exposed to very dry gas for long periods. This occurs as the electrolyte becomes progressively drier. The problem has been minimized through the addition of glycols and other proprietary components to the electrolyte [20] or by the cyclic addition of controlled amounts of water vapor in combination with flow modulation to keep the layer sufficiently wet [21]. However, even so, electrolytic phosphorus pentoxide hygrometers still respond relatively slowly to step changes and are more similar to capacitive sensors in this regard [22]. In recent years rhodium has been used for the electrodes rather than platinum, as platinum acts as a catalyst in a recombination reaction between chemisorbed hydrogen on the platinum and the oxygen product from the electrolysis. Electrolysis of the recombined water results in erroneously high water vapor measurements in oxygen and hydrogen matrices. The use of rhodium eliminates this recombination reaction. In addition, rhodium minimizes the tendency of metallic ions to migrate under the influence of the potential applied, which results in the formation of metallic compounds and the eventual bridging of the electrodes. Modern developments continue with respect to miniaturization and novel fabrication methods. Meeco manufactures a small low-cost phosphorus pentoxide-based monitor with a measurement range from 0.5 to 1000 ppmv. Manickam has reported a sensor for use at low flow rates (5 mL/min) in which the platinum electrodes were fabricated either with a pulsed-laser ablation technique or by screen printing. The thick-film screen-printed electrode version functioned for over 12 months and was able to detect moisture in argon down to 1 ppmv [23].

Phosphorus pentoxide electrolytic hygrometers can be used with all inert gases and many inorganic and organic gases that do not react with electrolyte. Gases that are compatible include nitrogen, oxygen, hydrogen, air, helium, neon, argon, krypton, carbon monoxide, carbon dioxide, methane, ethane, propane, butane, natural gas, Freons, fluorocarbons, and sulfur hexafluoride [24]. Specially designed units operated in amperometric mode and equipped with corrosion-resistant hardware are compatible with corrosive gases such as chlorine and hydrogen bromide [25]. However, measurements in corrosive gases are only possible down to single-digit ppmv

*Manufacturers and product names are given solely for completeness. These specific citations neither constitute an endorsement of the product nor imply that similar products from other companies would be less suitable.

levels, as only a fraction of the incoming water is electrolyzed, and electrolysis is diffusion limited. Gases that should be avoided include amines, ammonia, and certain unsaturated hydrocarbons (alkynes, alkadienes, and alkenes higher than propylene), which can polymerize and form liquid or solid residues that may block the cell.

7.3.2 Oscillating Quartz Crystal Microbalances

Oscillating quartz crystal microbalances (QCMs) are piezoelectric quartz crystals that have been coated with a thin film of a hygroscopic material which absorbs water vapor selectively from the sample gas passing over it. As the water vapor concentration increases, the water absorbed increases the weight of the film and decreases the oscillation frequency of the QCM, according to [26]:

$$\Delta f = -C_m \Delta m \quad (7.1)$$

where Δf is the change of the crystal resonance frequency resulting from a change in mass per unit surface area (Δm) and the constant C_m is a property of the crystal. Frequency-change measurements are made relative to a reference crystal that is not exposed to the gas stream. This compensates for temperature drifts and other external factors that similarly affect both crystals and enables high-sensitivity measurements down to low- and sub-ppbv levels. By alternating the flow of sample and dry reference gas over the QCM for short intervals (e.g., 30 seconds), the frequency difference due to water absorption during each cycle can be determined:

$$\Delta f = (f_{\text{sample gas}} - f_{\text{reference crystal}}) - (f_{\text{dry gas}} - f_{\text{reference crystal}}) \quad (7.2)$$

Because the frequency change is proportional to the gas-phase water concentration, a dedicated microprocessor collects the frequencies and calculates the concentrations using a polynomial expression obtained through prior calibration. During measurements, the period during which the sensor is exposed to sample gas flow is not sufficient to equilibrate the coating with water. However, the amount of water accumulated in a specific sampling interval is proportional to the water vapor concentration and can be used as a measure of the actual concentration during each sampling cycle (Figure 7.5a and b). The theory of QCM technology has been discussed and reviewed in more detail by O'Sullivan and Guilbault [27]. Instrument design and practical aspects of the technology for gas analysis are also covered in some detail by Wiederhold [24] and by Funke et al. [1].

Various hygroscopic coating materials that absorb water preferentially have been investigated for QCM analyzers, including zeolites, metal oxides, salts, and polymers [27–30]. Commercial QCM technologies typically use proprietary polymer coatings. Early units were introduced by DuPont Company and Shimadzu Corporation (Tokyo, Japan). Today, instrumentation manufacturers include Ametek Process Instruments (Newark, DE) and Mitchell Instruments (Ely, Cambridgeshire, U.K.). Figure 7.5, shows an Ametek 5800 QCM hygrometer, including a flow schematic with main components, the process measurement cycle and performance for ppbv-level water vapor detection in nitrogen. The QCM in this unit is an AT-cut quartz crystal operated

with a thickness-shear mode of oscillation at 9 MHz and temperature controlled at 60 °C. Filtered sample and reference gases at 200 mL/min are passed over the sensor sequentially in each measurement cycle.

A number of factors that to be considered when making measurements with QCM hygrometers. First, as measurements are made relative to a reference gas stream, a high-efficiency purifier (typically, a molecular sieve or other suitable material) must be used to generate a “dry” reference gas with a water vapor concentration well below the detection limit of the sensor. Second, as the amount of water absorbed on the sensor is dependent on temperature and pressure, control of these parameters within the analyzer is vital for accurate measurements, especially at low concentrations. Other factors to account for include differences in flow rate, line length, and gas composition between sample and reference streams. In the case of the latter, different sample and reference gas matrices can be used in some QCM systems by applying a correction factor that accounts for factors such as gas viscosity [17]. However, more accurate and sensitive results are typically obtained when the same sample and reference gas matrix are used. Users should also be aware that the absorption of water vapor by the QCM sensor is dependent on the material properties of the polymer film. Although sensors are quite rugged, these properties can change over time or can be affected by exposure to different sample gases. Therefore, periodic calibration of the sensor, as well as detection limit confirmation is required. Commercial systems typically include a permeation-based moisture generator that is integrated into the instrument sampling system and allow users to verify calibrations using a single concentration point (ca. 1 ppmv level). However, multipoint calibration and permeation tube replacement are advisable at least on an annual basis.

Detection limits for QCM instrumentation in specialty gases are typically in the low to single-digit ppbv range, with a dynamic range between 0 and approximately 2000 ppmv (Figure 7.5c). However, detection limits in the 150 pptv range have also been reported recently for specialized units used in inert matrix gases [31]. Response time is important for process monitoring applications. The speed of response to water vapor changes is relatively rapid compared to that of other sensor-based methods. Wet-up response periods of 80 % to a step change in less than 10 minutes have been reported at the 10-ppbv level. In other dry-down tests, for an external water vapor change from 50 to 23 ppbv (Figure 7.5d) the sensor reached 95 % of the final value in just over an hour. QCM hygrometers are compatible with various gas matrices, including inert gases, air, oxygen, hydrogen, nitric oxide, carbon monoxide, carbon dioxide, hydrocarbons (such as methane, ethylene, and propene), fluorocarbons (such as tetrafluoromethane or hexafluoroethane), nitrogen trifluoride, and sulfur hexafluoride. In addition, some reactive gases, such as silane and arsine, can also be analyzed [32]. Figure 7.6 shows a time plot of water vapor spiked into dry arsine from 22.6 ppbv to 1.8 ppmv and the corresponding graph of measured versus added water vapor using a QCM hygrometer. Due to the toxicity or flammable/pyrophoric nature of some reactive gases, the analyzer must be specially prepared to ensure material compatibility and leak-free operation of switching valves over time in the unit.

The technology is not suitable for use in corrosive gases or with gases such as ammonia that can strip off the polymer layer or otherwise degrade the sensor. In

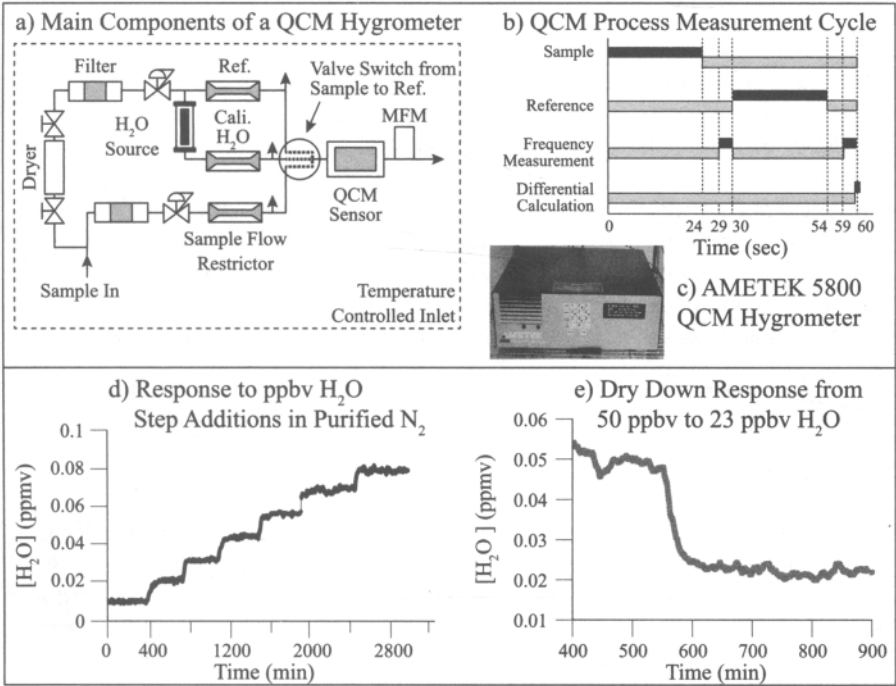


Figure 7.5 Main components, process measurement cycle, and wet-up and dry-down responses of a QCM hygrometer.

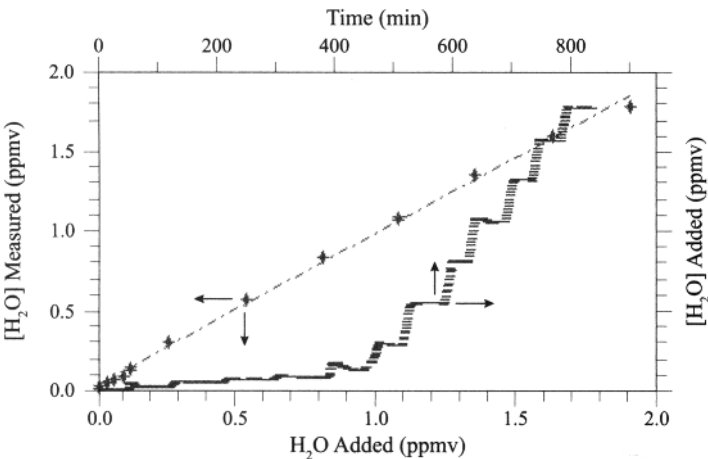


Figure 7.6 Measurement of water vapor in arsine using a QCM hygrometer (Ametek model 5800). Time plot shows water vapor addition to dry arsine (upper x and right y axes). The graph shows added versus measured water vapor in the concentration range 22.6 ppbv to 1.8 ppmv (lower x axis and left y axis).

such cases other approaches have been attempted. For example, a QCM sensor sputter-coated with barium metal has been demonstrated for water vapor detection in ammonia [33–35]. Since the barium reacts instantly and irreversibly with the water vapor, forming barium hydroxide and hydrogen, the mass of the coating increases, causing a decrease in the oscillation frequency that can be correlated to water vapor concentration based on a known gas flow. Although detection limits of less than 1 ppbv and approximately 10 ppbv moisture in nitrogen and ammonia, respectively, have been reported with such a sensor, it has not been used widely, for several reasons. First, the presence of ppmv levels of oxygen and carbon dioxide also react with the barium and affect the accuracy of the water vapor readings, and second, the irreversible reaction of the barium layer necessitates periodic replacement of the sensor.

7.3.3 Chilled-Mirror Hygrometry

Chilled-mirror hygrometers operate by measuring the dew-point (or frost-point) temperature of a flowing gas stream directly. The *dew point* is the temperature to which a volume of gas must be cooled at constant pressure for it to become saturated with respect to liquid water. Consequently, any cooling below the dew-point temperature causes the excess water to condense, and this can then be detected optically on a mirror surface. At the low-ppmv to ppbv water vapor levels typically present in many specialty gases, the excess water forms as ice, and hence frost-point temperatures are measured. Since the dew- or frost-point temperature is a fundamental thermodynamic property, chilled-mirror hygrometry is considered an absolute measurement method and is also used widely as a calibration and transfer standard [18,36]. Wiederhold discusses the approach in detail and provides dew-/frost-point/water vapor concentration tables [24].

A number of companies manufacture continuous-condensation chilled-mirror hygrometers, including Buck Research Instruments (Boulder, CO), Kahn Instruments (Wethersfield, CT), General Eastern Instruments (GE Industrial Sensing, Bellerica, MA), and MBW Elektronik AG (Wettingen, Switzerland). These instruments measure the dew-/frost-point temperature by regulating the temperature of the polished metal mirror and monitoring the light intensity reflected by the mirror (Figure 7.7). A high-brightness light-emitting diode is used as a light source, and the light reflected from the mirror is detected with a photodetector. The signal is fed into an electronic feedback control system that regulates the mirror temperature. When the mirror is above the dew-/frost-point temperature (no condensation) the intensity of light reaching the detector is maximized. As the mirror temperature is lowered below the dew-/frost-point temperature, water droplets or ice crystals form on the mirror and scatter the light, resulting in decreased light intensity reaching the photodetector. The frost layer thickness is typically displayed as a balance voltage. With a properly designed feedback control system, the mirror temperature is regulated such that the rate of condensation exactly equals the rate of evaporation, and the ice layer thickness remains constant. Under this condition the dew/frost on the mirror is in equilibrium

with water vapor in the gas, and the surface temperature of the mirror is precisely at the dew/frost point of the flowing gas stream.

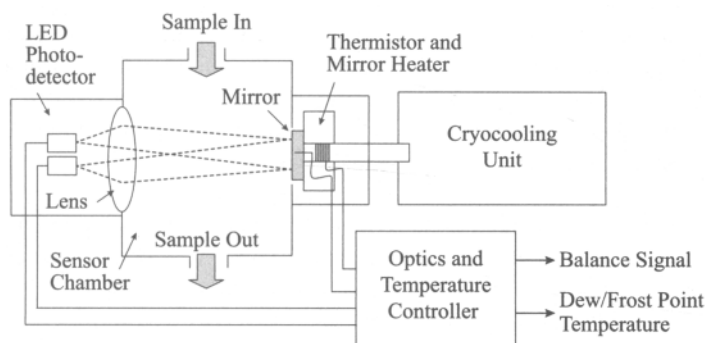


Figure 7.7 Principal components of a conventional chilled-mirror hygrometer.

The detection limit of a chilled-mirror hygrometer is based on the lowest mirror temperature that can be achieved by the cooling system or that can be reached before any matrix gas condensation occurs on the mirror (in the case of some specialty gases). Thermoelectric or Peltier cooling units used in many instruments cool the mirror down to -85°C (240 ppbv water in nitrogen). Other, more costly cryo-coolers are capable of cooling to temperatures below -96°C (30 ppbv water in nitrogen). The Kleemenko cycle cryo-cooler in the Buck Research CR-3 unit reportedly cools to -120°C , enabling detection below 1 ppbv. Care must be taken not to cool the mirror below the temperature at which the matrix gas condenses, as the ability to measure the dew point is lost at that point. Most hygrometers will allow a minimum mirror set-point temperature to be entered into the control unit of the instrument. Funke et al. discuss the case for analysis of phosphine and demonstrates water vapor detection at the 60 ppbv level [1]. In that work the mirror was kept above -86°C to prevent phosphine condensation (boiling point -87.7°C at 1 atm).

At sub-ppmv water vapor concentrations, several hours may be required before a suitable condensation layer is established. To hasten the process, a water vapor source can be pulsed into the flowing sample stream for a short period. Once a condensation layer is present, chilled-mirror hygrometers respond within minutes to changes in water vapor concentrations, although low-level readings may still take several hours to fully stabilize. As with other analysis methods, the sampling-manifold design, sensor chamber design, and sampling conditions may also affect equilibration times.

Several factors can affect the accuracy of measurements. First, it is important to minimize the error in the measurement of the mirror surface temperature at the point where condensation occurs. Therefore, high-end instruments employ precision NIST-traceable platinum resistance thermistors, embedded into the mirror surfaces, which have standard uncertainties below 0.1°C . Second, the presence of other contaminants can affect readings adversely. Particulate or volatile impurities other than water can collect or condense on a cold mirror surface and reduce mirror reflectivity. Therefore, a common practice is to open the feedback control loop periodically and heat the

mirror to a new “clean” state, then readjust the balance of the optical circuit to compensate for the reduced mirror reflectance. Even with rebalancing, some reactive gases, such as chlorine, ammonia, and oxides of sulfur, tend to react gradually with or dissolve in the water layer deposit on the mirror, forming an acid or caustic product that may decrease the vapor pressure (Raoult effect) and result in a higher-than-expected equilibrium dew-point reading [37]. Users should also be aware that at temperatures between 0 and -40°C , the dew layer may not convert to ice immediately or may exist indefinitely as supercooled dew. Supercooled dew tends to occur when the mirror is very clean, due to a lack of nucleation sites or because of certain types of mirror contamination. As misinterpretation of dew- versus frost-point data can result in significant errors, some chilled-mirror hygrometers have a “force frost” mode whereby the mirror temperature is lowered well below -30°C to form a frost layer and is then slowly increased to the true frost-point temperature. Other chilled-mirror hygrometers cycle the mirror temperature periodically to measure the dew point [24]. Cycling chilled-mirror hygrometers repeatedly lowers the mirror temperature at a precisely controlled rate until dew is detected, and then the mirror is heated to evaporate the dew before a continuous layer is formed. Typically, the measurement cycle is performed in 20 seconds. With this approach the buildup of contaminants on the mirror is minimized and measurement of the dew-point rather than the frost-point temperature is ensured. However, cycling parameters must be set carefully, and the instrument must be calibrated against a NIST-traceable hygrometer to ensure accurate measurements. Consequently, the method is employed more for industrial applications rather than as a laboratory calibration standard [18].

Chilled-mirror measurements can be made in a variety of nonreactive and reactive gases, including air, nitrogen, argon, helium, hydrogen, oxygen, hydrogen chloride, hydrogen bromide, and phosphine. When analyzing corrosive gases, corrosion-resistant sensor chamber components must be used to prolong the lifetime of the analyzer. For example, sensor housings are usually fabricated from stainless steel and the replaceable part of the mirror is made from an inert metal such as platinum or rhodium. Other custom modifications or materials related to the particular gas being analyzed may be required. As dew-/frost-point curves can be strongly matrix gas-dependent, curves generated in one gas are not generally applicable in another [38]. For example, interactions between water and corrosive gases such as hydrogen chloride and hydrogen bromide gases significantly increase the frost points by approximately 30 and 51.6°C , respectively, compared to nitrogen at the 1 ppmv moisture level (Figure 7.8). In comparison with phosphine, there is significantly less molecular interaction, resulting in only a minor positive shift of 4.8°C at the 1-ppmv level. Therefore, empirically derived calibration curves should be determined for each matrix gas of interest. Furthermore, chilled-mirror hygrometry is not applicable to all gases. For example, trace water vapor detection is not possible in gases such as ammonia and chlorine, which will condense on the mirror at temperatures corresponding to relatively high water vapor concentrations. However, in cases where it can be applied, the method offers significant advantages over other approaches, particularly with regard to its simplicity, accuracy, and fundamental measurement principle.

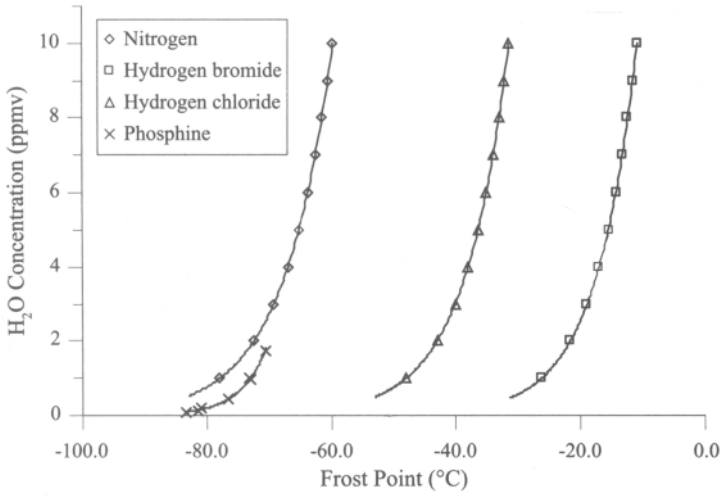


Figure 7.8 Plots of frost-point temperature versus moisture concentration in nitrogen, hydrogen chloride, hydrogen bromide, and phosphine matrix gases at 760 torr (101 kPa).

7.3.4 Capacitance-Based Sensors

Capacitance- or impedance-based sensors for water vapor analysis consist of a hygroscopic material that also functions as a dielectric and is situated between the two electrodes of a capacitor. Sensors based on aluminum oxide, silicon oxide, and porous silicon are commercially available. Materials for humidity sensors have been reviewed by Chen and Lu [39]. The most common capacitance hygrometer consists of a high-purity aluminum electrode that has been anodized to provide a porous oxide layer. A very thin gold coating is deposited over these structures to form the second electrode. During analysis, water vapor is transported rapidly through the gold layer and equilibrates in the aluminum oxide pore walls, affecting the dielectric constant of the material and as a result, the capacitance of the unit. The capacitance can be calculated according to

$$C = \epsilon\epsilon_0 \frac{A}{d} \quad (7.3)$$

where ϵ is the dielectric constant of the material, ϵ_0 is the vacuum permittivity, A is the overlapping area of the electrodes, and d is the distance between the electrodes. The large difference between the dielectric of the base material [$\epsilon(\text{Al}_2\text{O}_3) = 9$] and water [$\epsilon(\text{H}_2\text{O}) = 80.4$ at 20 °C] causes detectable changes in the capacitance, even though only small amounts of water adsorb on the dielectric from the gas phase. Resistive components of the hygroscopic layer are also affected by water adsorption, and hence commercial instrumentation typically measures the impedance (resistive, capacitive, and inductive component in an oscillating circuit) of the sensor and correlates changes with the appropriate calibration data.

Aluminum oxide sensors typically have a wide dynamic range and can be calibrated from low ppbv up to tens of percent water vapor. Their response is not affected adversely by flow rate or temperatures up to 100 °C. Further, they can be operated at high pressures, up to approximately 200 atm (ca. 20 MPa). However, monitoring of sampling conditions and application of appropriate calibrations, preferably in the matrix gas of interest, are required for accurate moisture response. Because aluminum oxide sensors have a linear response to dew-point temperature and a logarithmic response to water vapor concentration, dew-point temperature is often displayed on aluminum oxide sensor readouts. It should be noted that although the correlation between dew point and concentration is similar in inert gases such as nitrogen or oxygen, significant deviations are observed in other gases. Therefore, dew-point readings are best applied for relative measurements in the same gas matrix. Aluminum oxide sensors are typically used for analysis of water vapor in hydrocarbons, air, and bulk gases such as nitrogen, oxygen, and argon. They are also applicable in some hydrides and hydride–gas mixtures. However, they are not suitable for use in corrosive gases, such as chlorine or hydrogen bromide, which may react with the sensor materials.

Although these sensors offer advantages of low price, rugged design, and applicability to inline measurements at varying temperatures and pressures, they do require frequent calibration (every six months). Further, aluminum oxide sensors have traditionally suffered from slow response as well as drift (decreasing sensitivity) and dormancy issues [40] related to the intrinsic adsorption–desorption properties of aluminum oxide. Mehrhoff, for example, reported that after 11 days, the response of five aluminum oxide sensors decreased to 25 to 50 % of the true moisture level [41]. The decrease in sensitivity observed with time has been attributed to loss of sites for water adsorption, entrapment of water within the pores, and changes to the pore structure of the material [42,43]. To minimize such issues, recently developed aluminum oxide sensors have been fabricated with an integrated heating element so that the sensor temperature can be cycled periodically (Figure 7.9). In this approach, a temperature pulse is first applied to dry down the sensor, after which the sensor is allowed to cool down. The water concentration measurement is made based on the wet-up slope and resulting change in impedance [44].

Tests on one such sensor (Hygrotrace, GE Sensing, Billerica, MA) have shown good detection sensitivity (1.8 ppbv), accuracy (correlation coefficient of 0.9985 for measured versus actual water vapor concentration), detection limit (ca. 10 ppbv in nitrogen), acceptable wet-up and dry-down periods in the range 13 to 108 min (to reach 95 % of the final value), and good stability over 15 hours [45]. Thermally cycling the sensor is effective for low water vapor concentrations up to the maximum concentration specified (ca. 100 ppbv). However, once the heating step does not dry-down the sensor reproducibly, the accuracy of measurements decreases progressively as the water vapor concentration increases.

Silicon-based sensors are similar to aluminum oxide sensors, except that the dielectric material is either silicon oxide or porous silicon manufactured using silicon chip technologies. They have a wide dynamic range, from low ppbv to percent levels and operate independent of flow and at a pressure from vacuum to approximately 200 atm

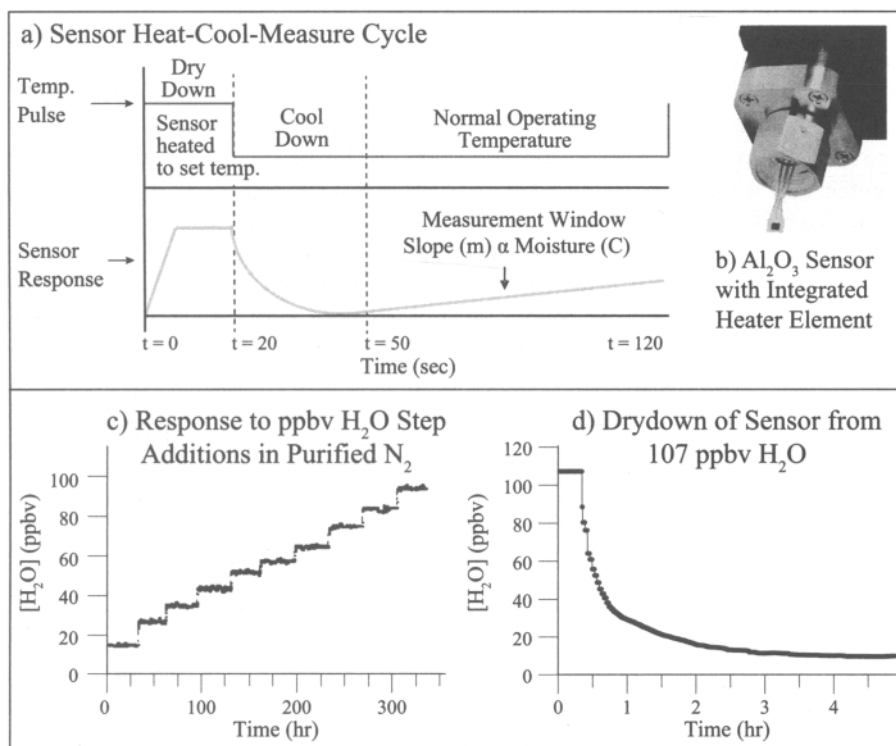


Figure 7.9 Operating principle and performance of a Hygrotrace aluminum oxide sensor in nitrogen: (a) time plot showing the heat–cool–measure step sequence of the sensor; (b) sensor chip with an integrated heating element; (c) response of sensor to water vapor step changes in the concentration range 15 to 93 ppbv; and (d) dry-down response at low ppb levels. The sensor took 108 min to reach 95 % of the final value from 107 to 10 ppbv.

(ca. 20 MPa). Although they are reported to drift less and have a faster response time than that of aluminum oxide sensors, they also require periodic calibration. Further, as their response is very temperature dependent, silicon-based sensors are typically thermostated. The sensor in the MAnalytical Microview hygrometer, for example, is held at 46 °C. It has an integrated heater that can also be used to increase the sensor temperature to 130 °C to desorb water when necessary and for rapid dry-down of a sensor from a wet condition. Silicon-based sensors are used for detection of water vapor in gases such as ethylene, natural gas, sulfur hexafluoride, hydrogen, air, and bulk gases.

7.4 Spectroscopic Methods

Spectroscopic methods have many advantages for the analysis of trace water vapor in process gases. These techniques not only offer rapid response times and high sen-

sivities but are also easily adapted for online monitoring applications because only optical access to the gas sample is required. Further, they can be applied to a wide range of matrix gases. FTIR is the most established technique in the field, enabling detection of multiple species, including water vapor. However, use of more selective near-infrared laser-based techniques such as TDLAS and CRDS has increased significantly within the last decade, due to development and commercialization of dedicated moisture analyzers. Other developing laser-based methods, such as broadband frequency-comb spectroscopy, are also considered to be promising candidates for next-generation multispecies analyzers. All of the methods discussed in this section are based on light absorption by the gas sample in a selected spectral region as a function of concentration of absorbing species according to the Beer–Lambert law:

$$I(\nu) = I_o(\nu)e^{-\alpha(\nu)LN} \quad (7.4)$$

where $I(\nu)$ and $I_o(\nu)$ are the intensity of transmitted and incident light, $\alpha(\nu)$ is the light absorption by a single molecule, L is the effective optical pathlength, and N is the density (number per unit volume) of absorbing molecules. Based on this relationship, in order to obtain the best absorption sensitivity, a strong molecular absorption line that is distinguishable from matrix gas absorptions and baseline variations should be chosen, and a long effective optical pathlength should be employed.

7.4.1 FTIR Spectroscopy

Operating Principles The operating principles of FTIR spectroscopy are discussed in detail in other publications [46–48]. Briefly, infrared radiation from a blackbody radiator is modulated in a Michelson interferometer (consisting of a fixed mirror, a moving mirror, and a beamsplitter), passed through a cell containing the gas to be analyzed, and then directed to an infrared light-sensitive detector (Figure 7.10a). The resulting interferogram, which is a plot of infrared intensity versus pathlength difference, is Fourier transformed to produce the infrared spectrum of absorbance versus wavenumber. FTIR spectroscopy is a single-beam method. Therefore, a background spectrum of the dried cell (and instrument bench) is first acquired as a reference, after which a spectrum of the sample is collected and referenced to the background spectrum to obtain the final absorbance spectrum. Because acquisition of a single spectrum takes less than a second, multiple spectra can be averaged in several minutes to increase the signal-to-noise ratio of each measurement. Quantitative results are obtained by relating the absorbance of moisture bands in sample spectra to those in calibration spectra of known standards, measured under the same conditions. Although FTIR spectroscopy is a mature technique, it should not be considered as a perfect “black-box” analyzer. Knowing where the limitations of performance arise and which components to optimize for trace analysis is critical to obtaining repeatable and accurate results [49]. These aspects are discussed further below.

FTIR Optical and Gas Sampling Components Although a variety of infrared sources exist for FTIR spectroscopy, silicon carbide glow-bars are an appropriate choice for the mid-infrared region. By varying the current through the glow-bar, it is

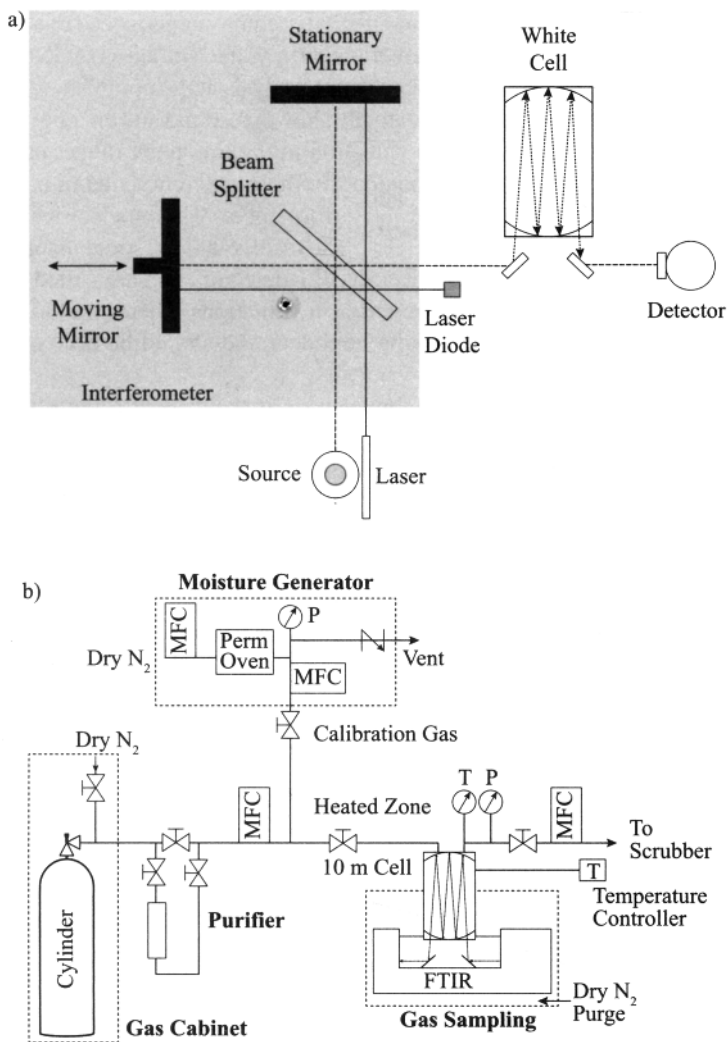


Figure 7.10 Schematics showing (a) main optical components and (b) gas-sampling components of an FTIR system for water vapor analysis.

possible to control the source temperature. Typical operation is at 1100 to 1200 °C, to ensure good sensitivity and lifetime. However, higher temperatures can be used for short durations to maximize the source intensity in the region 2200 to 4000 cm^{-1} when long path cells are employed. Other higher-temperature sources include zirconium oxide Nernst and molybdenum disilicide cermet sources. Potassium bromide is commonly used as a beamsplitter material. As potassium bromide is hygroscopic and will fog in the presence of atmospheric moisture, FTIR bench components must be kept under purge with dry nitrogen even when not in use.

FTIR detectors are selected based on sensitivity requirements, speed of acquisition, and wavenumber range [50,51]. Deuterated triglycine sulfate (DTGS) detectors operate at room temperature and can be used for analysis at the ppmv level. However, compared to other detectors they are relatively slow to respond and are not suitable for trace measurements. For water vapor detection in the low-ppbv range, narrowband liquid nitrogen-cooled indium antimonide (InSb) or mercury-cadmium-telluride (MCT) detectors currently offer the best performance. Thermoelectrically cooled indium arsenide (InAs)-based detectors are also available from some manufacturers. These detectors approach the sensitivity of MCT detectors and are suited for online FTIR applications where access is limited or in situations where liquid nitrogen is not available. Detector response may be nonlinear and should be accounted for in quantification [52].

Gas cells used for trace water vapor analysis usually have a multipass White design with multiple reflections of the light beam inside the cell to obtain a total pathlength of 5 to 20 m [53]. Some White cells have fixed pathlengths; others have adjustable pathlengths where the number of beam reflections is controlled by an external mirror adjustment. A 10-m cell provides high sensitivity, although the cell volume is normally rather high, on the order of 1 to 2 L. Users should be aware that at a flow rate of 1 L/min, each changeover in a 1-L cell will take 1 minute, and to flush a cell completely, at least five changeovers are required. Even then, water vapor measurements take longer to equilibrate, and this should be accounted for during sampling. Cells are constructed using chemically resistant materials such as glass, 316 stainless steel, nickel-coated alloys, or aluminum, fitted with gold-coated nickel mirrors and appropriate windows. The cell windows must not only be compatible with the gas to be analyzed but also provide the spectral transparency required for measurements. Potassium bromide is a commonly used window material, due to its wide transmission range (40,000 to 400 cm^{-1}) and compatibility with many nonreactive hydrides and corrosive gases. However, it cannot be used with gases such as chlorine, which result in anion-exchange reactions. In such cases other materials, such as quartz (50,000 to 2500 cm^{-1}) or calcium fluoride (66,666 to 1110 cm^{-1}), which may have a more limited transmission range, must be used. Calcium fluoride is also recommended for reactive fluorinated gases such as hydrogen fluoride, which will react with quartz. The properties of these and some other commonly used infrared transparent window materials are listed in Appendix B. O-ring materials can be metal or polymeric and should also be reviewed for gas compatibility, permeability, and outgassing in the case of the latter. Gas cells are thermally controlled and the cell temperature is chosen according to the sample gas properties. For example, some gases may decompose at elevated cell temperatures, while other gases, such as hydrogen fluoride, that hydrogen-bond have very temperature-sensitive infrared spectra [54,55].

The construction materials, design, and operating conditions of the manifold used to deliver the sample gas or water standards to the cell are similarly important to optimize (Figure 7.10b). Electropolished 316 stainless steel is widely used for manifold components and lines due to its compatibility with most gases. However, other alloys, such as Hastelloy, are used for some corrosive gases. Surface area and

dead volume in the delivery manifold are minimized to prevent long dry-down times, and regulators and sampling lines are thermally controlled (e.g., 60 °C) to prevent ambient temperature fluctuations from affecting the readings. Typically, gases are sampled dynamically through the cell at 0.5 to 2 L/min, and the cell pressure is controlled using an electronic pressure controller.

A key concern when making trace water vapor measurements by FTIR is the infrared absorption by water vapor in the beam path within the bench but outside the cell. Therefore, care must be taken to purge atmospheric moisture out of the bench to a negligible or low and steady level using purified nitrogen or other appropriate dry purge gas, so that the background can always be effectively subtracted from the spectrum of the sample. Several FTIR manufacturers, including MKS Instruments (Andover, MA), Thermo Scientific (Madison, WI), MIDAC Corporation (Irvine, CA), and CIC Photonics, Inc. (Albuquerque, NM), supply instrumentation specifically designed for online gas analysis that have optimized containment of bench and cell transfer optics for efficient purge of water vapor. In some cases the bench components can also be heated to assist with dry-down. Most other general laboratory FTIR instruments, in addition to the regular internal bench purge, require modification by placing the entire FTIR optical bench inside a sealed enclosure (i.e., a plastic purge box). This must be purged independently with a purified gas stream at sufficient flow rates (ca. 20 L/min dry nitrogen). Other approaches investigated to minimize or account for background water vapor include bench evacuation or the use of a specially designed optical system that allows sequential measurement of water vapor in the bench alone or in the gas cell alone to reference out the water vapor in the bench [56–59]. Note that auto- or self-referencing methods that are used for background spectral removal from within the gas cell (discussed in more detail in Chapter 3) still require a low and steady-state level of water vapor in the bench purge [60].

FTIR Operating Parameters Important parameters to optimize for trace water vapor measurement include spectral resolution, number of co-added spectra, scan time, and apodization function [47,48,61]. Several studies have shown that the best sensitivity is obtained using a spectral resolution of 2 to 4 cm^{-1} [56,57,62]. Higher resolution enables the absorption peaks of interest to be better resolved from those due to interfering molecules, but it results in an increased noise level and longer scan times. Lower-resolution measurements can be made more rapidly but suffer from a higher degree of spectral overlap, which can be a problematic with some sample gas matrices [62,63]. Because the signal-to-noise ratio of a spectrum increases with the square root of the number of spectral scans, the co-addition of a large number of spectra increases sensitivity. However, the increased sampling period can offset the benefit of lower noise levels. Consequently, for online water vapor analysis of flowing gas streams, a compromise between sensitivity and data acquisition rate must be reached. Typically, for low-ppbv detection of water vapor, each infrared data point is obtained from the co-addition of approximately 200 to 400 spectral scans collected in under 5 minutes.

Finally, the apodization function selected has an impact on spectra in terms of the spectral line width and the presence of side lobes. Clear differences in the spectra of

water vapor that have been processed with different apodization functions are evident [61]. Therefore, the same function must be used when processing calibration and sample spectra. The use of the Norton–Beer weak function is recommended for high resolution or when good quantitative analysis is required [47].

Spectral Region Selection and Quantification Method In the absence of matrix gas or cell window absorbance spectral overlap, water vapor can be quantified in two mid-infrared regions where strong water absorptions occur: 1900 to 1300 and 3900 to 3600 cm^{-1} . When analyzing gases such as hydrogen, argon, or chlorine that don't have permanent dipole moments, either region can be used, since they are infrared transparent. However, for other gases, a region free from matrix gas absorptions must be located for water vapor detection. Sampling of neat (100 %) matrix gas in long-pathlength cells invariably results in strong and broad matrix gas absorptions, many of which are off scale. This is not immediately apparent from library spectra, which are often measured with short-pathlength cells or with the gas at low pressure or diluted with nitrogen.

For many gases, including the hydrogen halides and the carbon and nitrogen oxides, one or both regions are available for water vapor analysis [54–59,64–66]. An example of the analysis of a low-purity nitric oxide sample is shown in Figure 7.11. Clearly, care is required to avoid regions where the matrix gas or other impurities, such as carbon dioxide (3550 to 3750 cm^{-1}), absorb. Many hydride gases, such as arsine, phosphine, ammonia, silane, and disilane, also interfere with detection of low-level water vapor in many infrared regions. Trace measurements are only possible by selecting very narrow spectral windows in which the absorbance bands for water and the matrix gas are strong and weak, respectively, and by using regression-based data analysis [65,67]. In ammonia, water bands in the region 3682 to 3988 cm^{-1} have been used to measure water vapor down to 10 ppbv [65,67–69]. Similarly, in arsine, there are several bands in the region 3660 to 3760 cm^{-1} that can be used. In phosphine, water vapor can be detected in narrow windows in either region, but bands between 1500 and 1570 cm^{-1} have the least interference from the phosphine matrix [70].

Quantification using classical least squares (CLS) is preferred in cases where matrix gas interference occurs [71–73]. With this approach, a spectrum of water vapor in nitrogen at a known concentration is added spectrally to that of the dry sample matrix gas until a match to the sample spectrum is obtained. The actual concentration of water vapor in the sample is then calculated from the individual contributions of the two spectra. The CLS method not only improves the analysis precision but also enables multiple components to be analyzed simultaneously. Further data on the residual spectra provide feedback to the analyst on the presence of interfering impurities in the region used for quantification. The success of the CLS method is dependent on the quality of the spectra used for quantification. As the sampling conditions (cell pressure and temperature, matrix gas type, and FTIR spectral collection parameters) can significantly affect the spectral line shapes, the spectra of purified matrix gas, calibration standards, and sample should be measured under the same conditions. This is discussed further in Chapter 3. Typically, FTIR detection limits for water

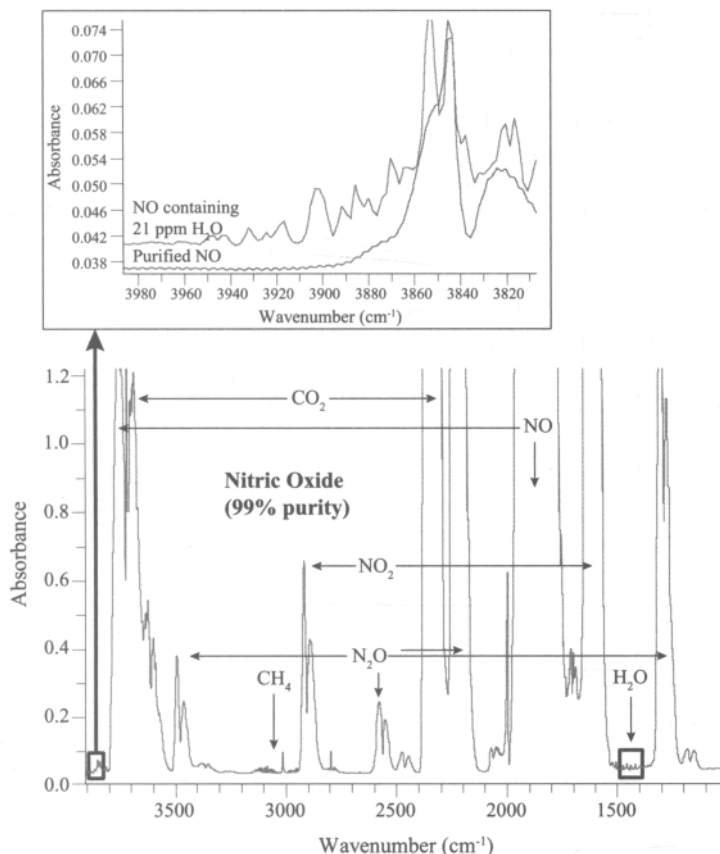


Figure 7.11 Infrared spectrum of nitric oxide (99 % purity) showing the presense of methane, carbon dioxide, nitrogen dioxide, nitrous oxide, and water vapor impurities. The upper insert illustrates infrared spectra of nitric oxide containing 21 ppm water and the same sample gas stream after passing through a purifier to remove the water.

vapor in many corrosive and hydride matrix gases are in the range 10 to 30 ppbv. To measure water vapor in reactive gases at single-digit and sub-ppbv levels in real time, more sensitive laser spectroscopy methods are required.

7.4.2 Tunable Diode Laser Absorption Spectroscopy

TDLAS is an established method for quantitative assessment of species in the gas phase. Its major advantages over other techniques are high selectivity, fast response, and ability to achieve low detection limits. These attributes are particularly important in microelectronic applications. Therefore, TDLAS has been used to detect water vapor in a variety of inert, corrosive, and reactive gases (including argon, helium, oxygen, nitrogen, hydrogen, hydrogen chloride, hydrogen bromide, chlorine, am-

monia, phosphine, dichlorosilane, nitrogen, tetrafluoromethane, nitrogen trifluoride, silane, and sulfur hexafluoride) [74–83].

Principles of Operation Like other spectroscopic methods, TDLAS is based on the absorption of light by the sample as a function of wavenumber, according to the Beer–Lambert law [equation (7.4)]. The main components of a TDLAS system include a diode laser light source, transmitting optics, gas sample and reference cells, receiving optics, photodiode detector(s), and associated control electronics and data system (Figure 7.12).

The sample in the gas cell attenuates the optical power from the laser in proportion to the analyte concentration and optical pathlength, and the relative attenuation of the optical power (ratio of the power measured with the sample present to the power measured in the absence of sample) is detected as the analytical signal.

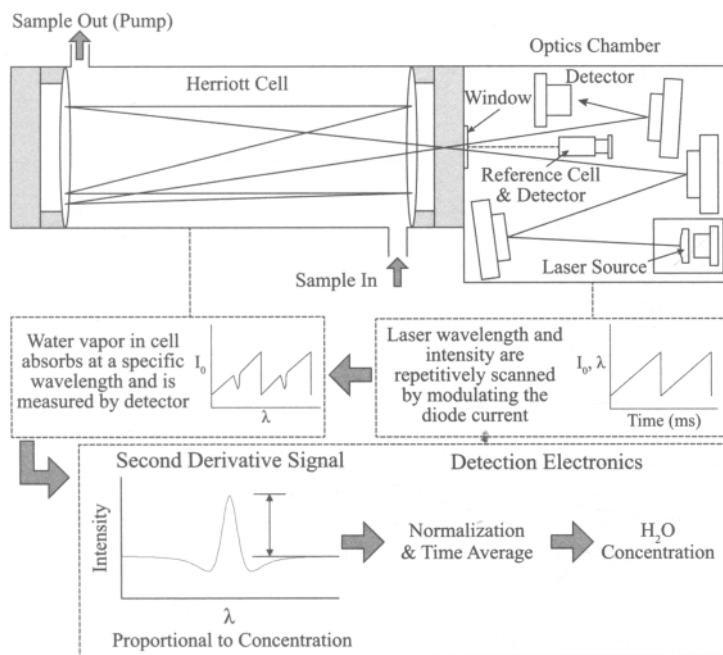


Figure 7.12 TDLAS schematic depicting the principle of operation and sensitivity enhancement using a $2f$ second-derivative absorption spectrum.

In TDLAS the amount of water vapor is measured by quantification of the absorbance of a single rotational line within a fundamental vibrational, a vibrational overtone, or a combination vibrational band of water vapor, and the selectivity of the technique stems from the precise overlap of the diode laser wavelength with the water absorption. The water absorption line is typically scanned by maintaining the laser at a constant temperature, sweeping the laser frequency with the drive current and measuring the decrease in laser power after passing through the sample. The ability

to measure low concentrations of the analyte is limited by noise present in the measurement background. However, the sensitivity of the TDLAS measurement can be improved significantly by the use of wavelength-modulation spectroscopy (WMS), which reduces the contribution of excess laser noise to the total noise current [74]. Signal-to-noise improvements of three orders of magnitude compared with direct absorption spectroscopy have been reported [84]. In WMS, the laser wavelength is slowly tuned over the absorption line and modulated simultaneously by rapidly varying the drive current at a frequency f . The resulting absorption signal is then demodulated by a phase-sensitive detector at the modulation frequency or at the first or second harmonics of the modulation signal ($1f$ and $2f$, respectively). The line shapes produced at the first and second harmonics are approximately the first and second derivatives of the original line shape, respectively. Wavelength-dependent features such as sloping backgrounds contribute to the first-derivative profile. For example, with a constant slope, these appear as a constant offset in the $1f$ case. However, such features are removed in the second-derivative profile while the sharp variations due to the actual sample absorption remain intact (Figure 7.12). It should be noted that background spectral features such as étalon interference fringes that tend to drift in time are not removed in WMS. The second-derivative profile is directly proportional to concentration and can be modeled explicitly according to known spectroscopic parameters of laser-tuning rate, modulation depth of the laser wavelength, and pressure-induced line broadening of the specific absorption to interpret the strength of the moisture signal. Optimization of spectroscopic measurements with modulation techniques, such as frequency modulation and two-tone modulation, are discussed and reviewed in several publications [85–87].

Effects of Pressure Broadening and Matrix Gas An important consideration with laser spectroscopic techniques is that the resulting line shape is dependent on the pressure-broadening effects of the matrix gas. At 760 torr (101 kPa), collisional broadening of absorption lines (due to intermolecular collisions between gas molecules) is the dominant line-broadening mechanism, giving rise to a nominally Lorentzian line shape with a width that is proportional to the total pressure. At low pressure (e.g., 10 torr or ca. 1.3 kPa), Doppler broadening is dominant (due to the Maxwell–Boltzmann distribution of molecular speeds), resulting in a Gaussian line shape. At intermediate pressures of 50 to 250 torr (7 to 35 kPa), a Voigt line shape, which is a convolution of Lorentzian and Gaussian features, is observed. Other important mechanisms influencing moisture line shapes are Dicke narrowing and speed-dependent broadening and shifting [88,89]. The systematic errors associated with pressure broadening are on the order of 10 % when a Voigt fit is used because the details of these linewidth effects are ignored, while the systematic errors associated with the total line strength (peak area) are less than 1 %. Detection in the intermediate pressure range is commonly employed to minimize interference from the matrix gas and to balance signal strength while keeping the line shape narrow enough that the full shape can be recorded within the wavelength scan of the laser. In different gas matrices there is a varying amount of broadening, so each gas must have an associated unique line measurement or calibration. Vorsa et al. reported measured

pressure-broadening coefficients for the 1392.53-nm water line in hydrogen chloride, hydrogen bromide, chlorine, and oxygen, which are, respectively, 2.76, 2.48, 1.39, and 0.49 times that of the nitrogen pressure-broadening coefficient [90].

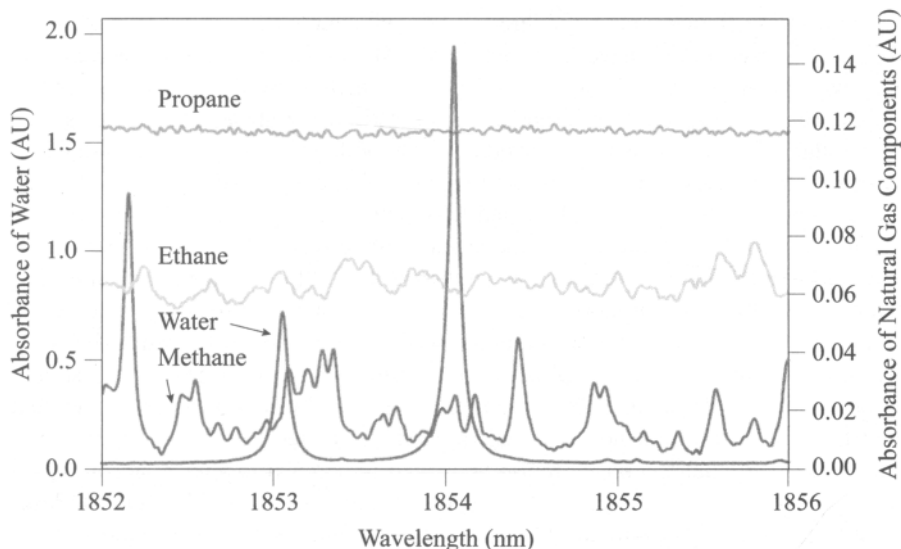


Figure 7.13 Spectra of methane, ethane, propane, and water vapor in the region 1852 to 1856 nm. Spectral overlap with water vapor exists for methane, but to a much lesser extent with ethane and propane. Reprinted with permission of ISA from [91].

Unlike broadband infrared sources, the emission of diode lasers provides a strong signal with an extremely narrow linewidth, on the order of 10^{-3} cm^{-1} or smaller. This greatly facilitates the resolution of the sample absorption from those of the matrix gas or other potentially interfering species at nearby wavelengths. However, even so, some gas matrices (in particular, hydrides such as ammonia, phosphine, arsine, and methane) absorb in many of the same wavelength regions as that of water vapor (Figure 7.13). Therefore, it is important not only to select a suitable water line in a region where matrix gas absorbance is minimized, but also to account for any matrix gas absorbance contribution to the water reading [76,91]. Double-beam acquisition and subtraction is one way to account effectively for matrix absorption [76]. With this approach, a reference cell containing a purified stream of the matrix gas is employed to remove absorbance lines from the gas matrix, cancel common-mode noise from the diode laser, and remove the contribution of atmospheric moisture absorption outside the sample cell. This, together with the second-derivative absorption signal to remove the impact of laser beam intensity variations induced by laser wavelength sweep, enables low-ppbv detection limits. Much of the work on dual-cell TDLAS has been reported by Wu et al. They developed a system for water vapor analysis in nitrogen, ammonia, and hydrogen chloride, based on an indium gallium arsenide phosphide (InGaAsP)–distributed feedback (DFB) diode laser emitting at 1380 nm.

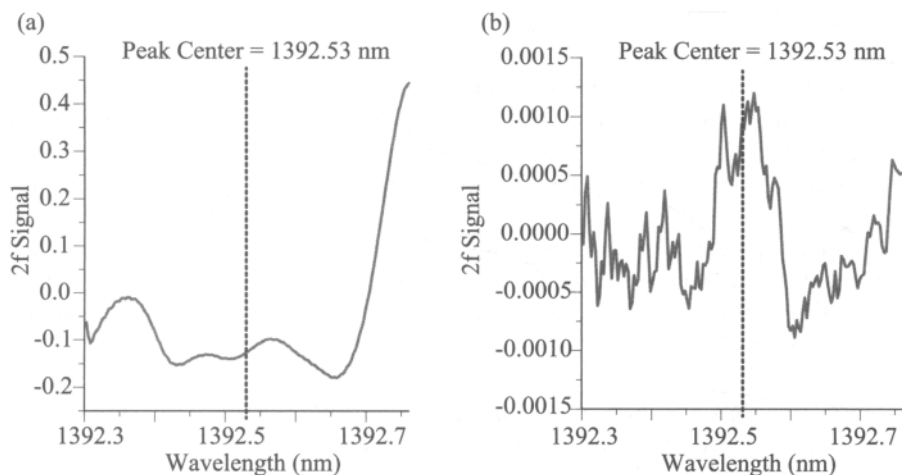


Figure 7.14 Absorption of water vapor in ammonia. (a) Superimposed spectra of 21.9 to 29.2 ppbv water vapor in ammonia, where spectra are dominated by ammonia absorption features, and (b) subtraction result from the spectra in (a) showing detection of water vapor at about 7 ppbv (note difference in the scales in the spectra). Reprinted with permission [78].

In the case of hydrogen chloride, water vapor was detected down to less than 20 ppbv in a 50-cm cell at 60 torr (8 kPa) using the line at 1380.64 nm [76]. For ammonia, the water vapor impurity could be detected down to 12 ppbv using a 92-cm pathlength cell and a laser, tuned from 1370.93 to 1370.99 nm at room temperature [75].

As the dual-cell arrangement is instrumentally complex, and it is difficult to maintain the necessary balance between the two beams over time, most TDLAS systems are equipped with only a single cell. In this case, if there are matrix gas absorption contributions at the wavelength used for water vapor measurement, then the spectrum of a purified gas stream must be generated, modeled, and used as a reference. This can be subtracted from that of the sample [78], as shown in the example for water vapor in ammonia in Figure 7.14. However, to make accurate measurements, the sample pressure must be tightly controlled at the pressure used to generate the reference. Outside this pressure range, water vapor readings can deviate significantly from the true water vapor content, as the line-fitting routine ceases to account accurately for the line-broadening effects. For example, increasing water vapor readings on a Delta F DF740 ammonia analyzer (hardware described in more detail below) are observed as the cell pressure decreases from the pressure recommended (70 ± 3 torr or 9.33 ± 0.40 kPa), and vice versa. If the pressure is lowered progressively by 10 torr (1.33 kPa) and then 20 torr (2.66 kPa), the respective water vapor reading increases by approximately 10 and 250 ppbv [80]. Therefore, use of an electronic pressure controller is recommended in such cases.

In addition to the importance of pressure control, TDLAS users should be aware that any change in gas matrix composition (even a minor change) can also significantly, affect water vapor readings due to line broadening of the ammonia spectral

features in the background. This can occur during the generation of calibration standards when known water vapor concentrations in an inert gas such as nitrogen are spiked into dry matrix gas such as ammonia. Data reported by Funke et al. show that replacing ammonia with up to 5 % nitrogen results in an instrument response twice as high as that expected and, further, that the response to increasing nitrogen concentration in ammonia is linear with a slope of approximately 10 ppbv apparent water vapor per percent of nitrogen added to the dry ammonia. Generating a nitrogen-free calibration is possible for compressed liquefied gases if a cylinder with known water vapor concentration in the liquid phase is available. This can be inverted and a fraction of the vaporized stream mixed with purified gas to generate the concentrations required [80].

Review of TDLAS Systems, Applications, and Performance TDLAS systems have been developed and used for trace water vapor analysis since the mid-1990s. Inman and McAndrew first reported low ppbv sensitivities for water vapor in nitrogen (1 ppbv) and hydrogen chloride gases (3 ppbv) by use of the water vapor absorption line at 1456.888 cm^{-1} [79]. Their TDLAS setup used second-derivative detection and signal averaging and was calibrated directly by introduction of a water vapor standard into a 30-cm Herriott cell with a 9-m optical pathlength. The cell was operated at a pressure of 20 to 40 torr (2.66 to 5.32 kPa) so that the signal due to water vapor in the cell could be distinguished from the broader absorption from water vapor in the optical path outside the cell. The ultimate detection limit of the system was 10 ppbv water vapor in dry nitrogen and 63 ppbv water vapor in dry hydrogen chloride. A similar TDLAS system was used for online monitoring of water vapor in gases (hydrogen chloride, hydrogen bromide, tetrafluoromethane, nitrogen trifluoride, ammonia) supplied to process tools used to make microelectronic devices [77,81].

An early commercially available TDLAS analyzer used for semiconductor gas applications was developed in prototype form by Southwest Sciences, Inc. This system is based on a hermetically sealed laser chamber containing an InGaAsP diode laser source emitting at 1392.5 nm and tuning optics, connected to approximately a 1-L stainless steel Herriott multipass cell (50-m pathlength) fitted with sapphire windows. Tests in nitrogen at 100 torr (13.3 kPa), performed with the NIST low-frost-point hygrometer [24] and using moisture challenges in the range 5 ppbv to 3 ppmv range demonstrated sub-ppbv noise levels, residual moisture in the low ppbv range, and a 3σ detection limit of 3 ppbv [74]. Commercial versions of this system developed by Delta F Corporation (now Servomex) with a more compact optical design to reduce outgassing and incorporation of a water reference to prevent the laser drifting off the moisture absorption line show comparable sensitivity [78,80]. The DF740 unit for moisture analysis in ammonia has approximately 2 to 4 ppbv sensitivity and a 3σ detection limit of 9 ppbv. The unit for use in hydrogen chloride (DF730) has a reported sensitivity of 0.25 ppbv and a detection limit of 1 ppbv water [82].

The initial success of early TDLAS analyzers has encouraged the development of other commercial systems for continuous real-time monitoring applications. Ametek

Process Instruments, GE Sensing and Inspection Technologies, and SpectraSensors, Inc. have all developed process analyzers for the detection of water vapor in natural gas and hydrocarbons in the range from several thousand ppmv down to single-digit ppmv levels [91,92]. The Ametek 5100 unit is based on a DFB diode laser operating with a wavelength centered at 1854 nm. Detection of water vapor in natural gas has been reported down to the 4 ppmv range using a 90-cm pathlength cell at 760 torr (101 kPa) and 21 °C and second-derivative measurements [91]. Siemens Applied Automation has reported a LDS6 TDLAS process analyzer for in-situ measurement of water vapor in chlorine streams [93]. Other instrumentation will undoubtedly be developed as analytical needs arise in the future.

TDLAS is being used increasingly for in-situ monitoring and process control in a variety of gas applications [94] because of its ppbv sensitivities for water (assuming that absorbance lines without spectral interference from the matrix gas are available) and its ability to handle corrosive or aggressive gas environments [76,81,82,93]. The technology is rugged provided that the materials used for the gas-wetted parts are selected correctly for the gas being analyzed. TDLAS is less likely than CRDS to suffer performance losses due to particulates that can coat mirror surfaces of long-pathlength gas cells. However, mirror surfaces must still withstand the corrosive nature of some gases, such as hydrogen chloride, hydrogen bromide, or chlorine. TDLAS is also capable of responding rapidly to changing water vapor concentrations. Although the response time of TDLAS systems will vary depending on cell volume, flow rate, and sampling system design, readings typically equilibrate rapidly. Equilibration to 90 % of the final reading for a roughly 150-ppbv water step change can be expected within 5 to 10 minutes, depending on whether the analyzer is being wet-up or dried-down [80,82].

7.4.3 Cavity Ring-Down Spectroscopy

Principles of Operation In CRDS, the time dependence of the decay of light intensity in an optical cavity is used to measure absorption losses associated with a gaseous impurity and thereby calculate the impurity concentration. The gas under test flows through a resonant optical cavity illuminated with light absorbed by the impurity, in this case water vapor. A schematic of the basic elements is given in Figure 7.15. When the laser wavelength is in resonance with the cavity, a strong optical field builds inside the cavity, and a small amount of that light passes through the right-side mirror (sometimes called the “output coupler”) and is measured by the photodetector. When the incident light is turned off with the optical switch, the optical intensity in the cavity decays with a characteristic time constant τ . This time constant is determined by the total optical losses in the cavity, including the mirror transmittance and any absorption by the host gas and impurities. The cavity lifetime is determined by fitting the detector output with a simple exponential decay.

The number density of absorbing molecules, N , in the optical beam path inside the resonant cavity is given by the simple relationship

$$N = [c\sigma(\nu)]^{-1} [\tau(\nu)^{-1} - \tau_0(\nu)^{-1}] \quad (7.5)$$

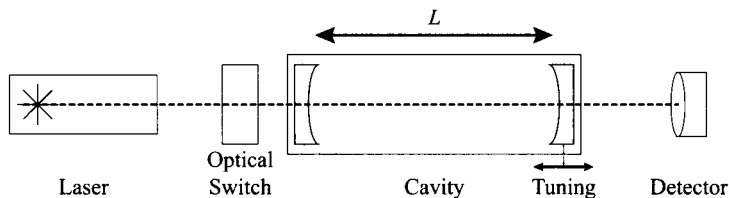


Figure 7.15 Basic elements of a CRDS system. The resonant cavity has length, L , defined by the two cavity mirrors.

where c is the speed of light, ν is the frequency of the laser light, σ is the absorption cross section for each molecule, τ is the measured lifetime, and τ_0 is the lifetime when no impurity absorption is present. In an ideal cavity, $\tau_0 = L/[c(1 - R)]$, where R is the geometrical mean of the reflectivities of the cavity mirrors (i.e., the square root of the product of the two reflectivities).

The absorption cross section is a function of the laser frequency, and for an isolated transition it can be modeled in terms of the line shape parameters (e.g., frequency, line intensity, broadening parameter, Doppler width). Most laser linewidths (typically, 1 MHz) are orders of magnitude smaller than the width of a pressure-broadened gas absorption line (typically, 1 to 3 GHz), and the width of the optical cavity resonance is usually even smaller still (ca. 1 kHz for a high-finesse cavity). Thus, application of equation (7.5) requires knowledge of the line shape for the gas absorption line and the exact position of ν relative to the center of the absorption line, ν_0 . For research measurements, the usual approach is to scan ν over a large range to achieve “zero” absorption at the ends and then fit the entire gas absorption peak to extract total absorption line strength, S , and estimate the proper background absorption. This process is most conveniently executed by first converting the τ values into absorbance, $\alpha(\nu)$, using $\alpha = (c\tau)^{-1}$. The most common line shape used for fitting gas absorption lines is the Voigt function, a convolution of a Lorentzian function, representing pressure broadening from intermolecular collisions, and a Gaussian function, representing the Doppler width of the transition for a particular temperature. Because the Gaussian width can be calculated from the Doppler broadening, this parameter can be held constant during the Voigt fit. For data acquired in air or nitrogen, the Lorentzian width can be determined from the AGAM value for water in the high-resolution transmission molecular absorption (HITRAN) database and also held constant. More complicated line shape functions are recommended for the highest accuracy, as discussed in Section 7.4.2.

An example of such a fit for water absorption in nitrogen gas is given in Figure 7.16. While the height and width of the absorption peak will change with environmental conditions, most notably total gas pressure, the integrated area under the line shape will remain constant. The Voigt line shape is parameterized in different ways depending on the analysis software used, but the fitting parameters are used to determine an integrated peak area A that has units of frequency (or wavenumber) divided by length, 4.57×10^{-5} MHz/cm in the example. The number density of water molecules can

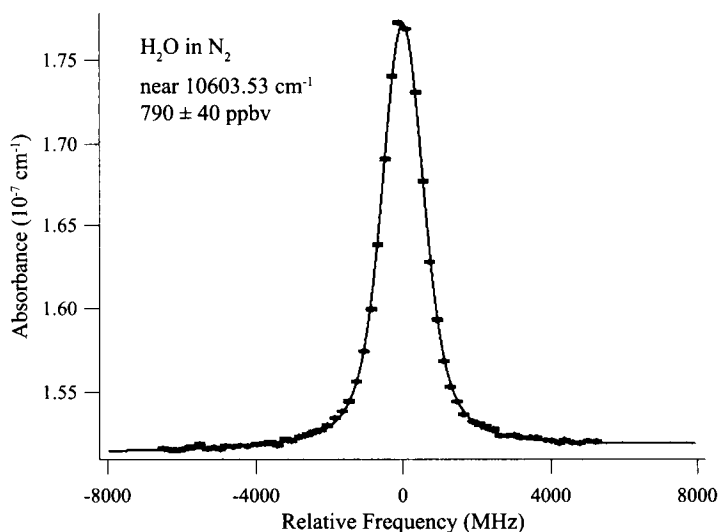


Figure 7.16 Curve fitting of water vapor absorption line in nitrogen carrier gas as measured by CRDS for a total cavity pressure of 13.3 kPa (100 torr) at room temperature. The cavity length is 73.5 cm. The instrument used to acquire these data is described in more detail by Lehman et al. [95].

then be extracted as $N = A/S$. The absorption line intensity, S , is typically reported in units of $\text{cm}^{-1} \text{cm}^2 \text{molec}^{-1}$, for example, in the HITRAN database [96]. For water vapor, there are several references [97,98] covering limited frequency ranges that include newer data than are generally reported in HITRAN. Converting the units of the published value [98] of $S = 5.899 \times 10^{-22} \text{cm}^{-1} \text{cm}^2 \text{molec}^{-1}$ with $1 \text{cm}^{-1} = 30 \text{GHz}$ yields $S = 1.77 \times 10^{-17} \text{MHz cm}^2 \text{molec}^{-1}$, and from the example curve we calculate a water molecule density of $2.58 \times 10^{12} \text{molec cm}^{-3}$. The uncertainty in peak area returned by the fitting program provides an estimate for number density uncertainty of $3 \times 10^9 \text{molec cm}^{-3}$. The water vapor mole fraction in the gas is given by the ratio of number density of water molecules to the total number density of gas molecules in the cavity, N_{tot} , which in turn is generally calculated from the cavity gas pressure P and temperature T using the ideal gas law ($PV = nRT$), where R is the gas constant $8.31 \text{J mol}^{-1} \text{K}^{-1}$. Multiplying the result by Avogadro's number (6.02×10^{23}) will convert moles to molecules, and for the example above, we arrive at a volume mole fraction for water vapor of $790 \pm 40 \text{nmol mol}^{-1}$ (ppbv). The larger relative uncertainty in the concentration compared with the water molecule number density arises because the chamber pressure and temperature vary under laboratory conditions, which in turn generates 5 % uncertainty in the total number density of molecules in the cavity.

For faster data acquisition, it is often sufficient to measure the peak absorbance (or some other convenient point on the curve to which a feedback circuit will lock) and check the background level periodically at a frequency far off from the peak. The line shape of gas absorption peaks is stable under conditions of constant temperature and pressure, and the total peak area is conserved when pressure variations broaden the curve. The Gaussian width of the peak arises from the Doppler broadening of the absorption line, and therefore is to first order independent of pressure, while the Lorentzian broadening arises from molecular collisions and therefore shows significant pressure dependence. Corrections can usually be made for pressure variations through the application of the pressure-broadening coefficient, defined as a proportionality coefficient between the Lorentzian half-width at half-maximum for the absorbance and the total pressure. Typical values are 30 to 60 MHz/kPa [90,95]. The challenges of determining the background level are discussed further below.

System Design Considerations

Cavity Design The optical cavity typically consists of two collinear mirrors, although designs based on prisms also have advantages for some applications [99,100]. The relevant cavity parameters for a linear cavity are summarized in Table 7.1. Although in principle cavity mirrors can be flat, greater stability and optical coupling can be obtained with mirrors that have a slight radius of curvature. A common configuration is one in which the cavity length is approximately 0.75 times the radius of curvature of the mirrors. Optical cavity design for CRDS is covered in detail by Busch et al. [101]. Mirrors with very high reflectance can now be obtained for the near infrared, based on careful evaporation of dielectric stacks. In fact, optimization of high-reflectivity mirror coatings was the first application of CRDS [102]. Low-

Table 7.1 Characteristics of a linear high-finesse optical cavity, with typical values based on cavity length of 75 cm and mirrors with reflectivity of 0.99993 %

Parameter	Equation	Typical Values	Comments
Free spectral range, ν_{SFR}	$\nu_{\text{SFR}} = c/2L$	200 MHz	Spacing of longitudinal cavity modes
Finesse, f	$f = \pi R^{1/2}/(1 - R)$	105,000	
Effective length, L_{eff}	$L_{\text{eff}} = 2Lf/\pi$	51 km	Length of a single path with the same total absorption
Background, τ_0	$\tau_0 = L/[c(1 - R)]$	83 μs	
Resonance width, $\Delta\nu$	$\Delta\nu = c/(2Lf)$	1.9 kHz	Full width at half maximum

loss mirrors produce a long τ_0 and therefore enhance the minimum sensitivity of the CRDS system. Because the detector sensitivity and response period will limit the ability to measure high impurity concentrations (with high absorption and short τ), the dynamic range of the impurity measurement is also enhanced by high-reflectivity mirrors. The cavity resonance width becomes narrower, however, as the mirror reflectivity increases, which increases the demands on laser frequency stability and mechanical stability for the cavity. Using cavity supports with minimal thermal expansion (Invar metal), limiting thermal variations, and isolating the system from vibration all lead to greater stability. Most high-finesse CRDS cavities are also equipped with a feedback circuit that either tunes the laser frequency to match the cavity or slightly adjusts the cavity length with a piezoelectric actuator on the mirror or cavity end supports and stabilizes the cavity related to a frequency reference such as a frequency-stabilized helium–neon laser [103]. Cavity optics should also be designed to minimize coupling to parasitic cavities formed by collinear mirrors, detector windows, front and back surfaces of mirrors, and so on. Thermal expansion and other drift in these components can generate variations in τ_0 over time and add to uncertainty in absolute concentration measurements [104].

Light Sources and Detectors The basic requirements for a light source are short-term stability and a tuning range over at least the molecular absorption line of interest. Three fundamental vibrational bands of water, designated as ν_1 , ν_2 , and ν_3 , and corresponding to wavelengths of 2.73, 6.27 and 2.66 μm , respectively, comprise thousands of rotational–vibrational transitions that have the potential to yield high sensitivity and selective measurements. The strongest transitions in these bands have room-temperature intensities over $10^{-18} \text{ cm}^{-1} \text{ cm}^2 \text{ molec}^{-1}$. However, the absence of laser light sources and sensitive detectors in this range has meant that most work has been carried out in the overtone bands near 0.9 and 1.4 μm (10,600 and 7000 cm^{-1} , respectively), where intensities are orders of magnitude weaker than those of the fundamental bands. Tunable laser sources for these bands include distributed feedback Bragg reflector diode lasers and external cavity diode lasers. The stronger molecular lines at longer wavelengths are becoming increasingly accessible with the development of optical parametric oscillators (OPOs) that combine laser sources operating in the near infrared (ca. 1 μm) and nonlinear optics to generate coherent light with overlap to the 1.8- and 3.2- μm water bands. Quantum cascade lasers are now commercially available with wavelengths greater than 4 μm , and these have been used successfully in CRDS systems [105,106]. Distributed feedback laser diodes have also been used in the near infrared to improve the compactness of CRDS systems [107]. In general, these coherent light sources are continuous wave (CW), which simplifies analysis of the ring-down signal, but single-mode cavity excitation can be achieved with pulsed sources by working with relatively short ring-down cavities [108,109]. A recent development in laser technology has been the frequency-comb laser, and its application to cavity ring-down spectroscopy and cavity-enhanced absorption spectroscopy is discussed elsewhere in this chapter.

Detectors must be chosen to have a response time well below that of the minimum τ to be measured. A high-finesse cavity can have an empty-cavity time constant

τ_0 of hundreds of microseconds, which is readily measured with semiconductor photodiodes provided that the detector area is kept small. Of the bands discussed above, only those near $0.9\ \mu\text{m}$ are detectable with silicon photodiodes; InGaAs, InAs, InSb, and HgCdTe detectors are employed most commonly for the longer wavelengths. As the bandgap of the photodiodes decreases, thermal noise and shunt resistance become more significant, requiring design trade-offs between sensitivity and response period relative to the specific target molecules and gas. Detectors also must operate with DC coupling over a dynamic range of three or four orders of magnitude to allow accurate τ measurement. If the detector signal is digitized, the electronics must also be capable of high resolution to cover the full dynamic range of the detector (analog-to-digital signal with 12-bit or higher resolution) [110].

Optical Components The optical switch in Figure 7.15 is typically an acousto-optic modulator (AOM) oriented so that the first-order diffracted beam is directed to the CRDS cavity. AOMs have fast switching times ($<100\ \text{ns}$) for small spot sizes and therefore do not affect the measurement of the decay time constant. A semiconductor optical amplifier can perform a similar function [111]. Other methods, such as detuning the laser, can also be employed as a switch, but often any laser adjustment increases undesirable chirp in the laser frequency during ring-down measurements. When the cavity is in resonance with the laser light wavelength, the cavity throughput is high as measured on the detector. The detector signal with suitable processing can serve as a trigger signal to turn off the cavity illumination via the optical switch. The same trigger signal can also start acquisition of the ring-down signal.

An optical Faraday isolator is usually inserted between the laser and the cavity to avoid reflection of the light from the front cavity mirror back into the laser source. This reflection is quite strong when the cavity is off-resonance and can interfere with laser stability. If the laser does not produce a clean Gaussian beam, coupling to only a single TEM₀₀ mode of the cavity will be difficult or impossible. A spatial filter or single-mode optical fiber can be added to the laser path to prevent excitation of higher-order cavity modes. A video camera or beam profiler that responds to the laser frequency is very useful for monitoring the mode patterns in the cavity during alignment. Finally, it will be necessary to measure the frequency of the light accurately. For frequency-stabilized cavities, it is often sufficient to tune the laser through successive longitudinal modes of the cavity and use the known position of the gas absorption line to place these changes on an absolute wavelength or wavenumber scale. Interferometric wavemeters are now commercially available with 0.2 ppm resolution in the near infrared, or 0.06 GHz for the laser frequency in the example spectrum, which is sufficient for acquisition of full line spectra. Although not necessary to the measurement, a Pound–Drever–Hall locking feedback system to the laser [112] will improve control over the acquisition of ring-down data. This lock mechanism requires additional optics to modulate the beam to produce an error signal for feedback on the cavity, and electronics to suspend feedback during retuning of the laser [113,114].

Review of CRDS Systems, Applications, and Performance The primary appeal of CRDS as a method to measure water vapor contamination in gases is that unlike most other methods based on optical absorption, CRDS does not rely on accurate measurement of light intensities. CRDS systems therefore do not require periodic calibration to correct for degradation of optical components or drifts in light source intensity and photodetector sensitivity. This method can also achieve less than 1 ppbv sensitivity and short measurement periods (<1 s). Although more sophisticated systems can occupy a large optical bench, the basic elements can be selected so as to fit inside a benchtop instrument enclosure. Water vapor analysis systems based on CRDS are now commercially available.

To a large degree, the history of CRDS development tracks the development of laser light sources. The method was developed initially with pulsed dye lasers. These sources produce a pulse train with a low duty cycle (1 to 10 Hz) operating at multiple frequencies due to the broad gain response of the dye relative to the laser cavity mode spacing. This method was used successfully to measure transition strengths for forbidden transitions in molecular oxygen, with an estimated absorbance sensitivity of 10^{-8} cm^{-1} [115]. Absorbance sensitivity on the order of 2×10^{-9} to $7 \times 10^{-10} \text{ cm}^{-1}$ was reported for the measurement of weak absorption lines in hydrogen cyanide [116]. The short duration of the pulse relative to the round-trip time period of the circulating beam meant that the cavity operated in a regime where light could be coupled into the resonator regardless of the wavelength detuning of the probe laser relative to the cavity resonances. Using frequency-domain analyses of the intracavity field, Hodges et al. [117], Lehman and Romanini [118], and Looney et al. [109] showed that for short pulse lengths ("long cavities"), there will be complications caused by mode beating effects and multiexponential decays in ring-down signals. For long pulse lengths ("short cavities") single-mode excitation of the ring-down cavity results, leading to exponential decay signals [108]. For pulsed excitation, the laser bandwidth can yield significant systematic error in the spectra measured and hence in the concentration deduced for the light-absorbing species [119]. In subsequent years, these multimode effects in CRDS were largely mitigated by the use of narrowband CW probe lasers. As these tunable sources became more widely available, CW-CRDS became more widespread, in part due to the simpler form of the underlying theory and data analysis. Detection limits on the order of 10^{-9} cm^{-1} were demonstrated in the measurement of weak acetylene overtones in the vicinity of 570 nm [120]. Heterodyne detection techniques were also shown to offer high sensitivity, on the order of 10^{-10} to 10^{-13} cm^{-1} , by overcoming technical noise sources, such as laser instabilities, acoustic noise, and electromagnetic noise from laser power supplies [110,121]. Most recently, frequency-comb lasers have also been employed as CRDS light sources in a very broad wavelength range [122]; this topic is discussed Section 7.4.4. An informative and more complete discussion of the historical development of CRDS may be found in other publications [123,124].

Advances in CRDS instrumentation are typically demonstrated for dilute analytes in vacuum or inert gases such as nitrogen. New practical considerations arose as the method was developed for commercial use to detect water vapor as an impurity in host gases (or matrix gases). Many of these gases have complicated spectra with a

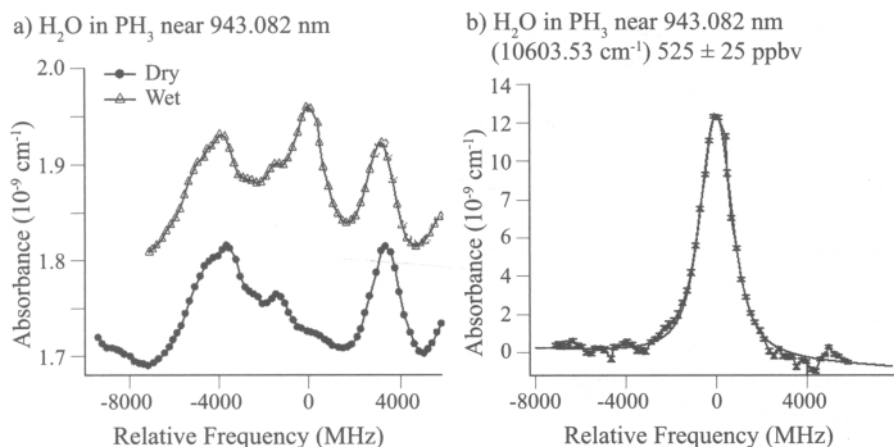


Figure 7.17 CRDS spectra for water vapor in phosphine gas. (a) Absolute absorbance scale showing spectra with and without water vapor present. The frequency scale zero corresponds to the position of the water absorption peak; other peaks in the spectra are weak phosphine absorption lines. (b) Curve fit of the peak obtained by subtracting the “dry” phosphine spectrum from the “wet” phosphine spectrum. The instrument used is the same as that used to acquire the data in Figure 7.16.

high density of overtones and broad backgrounds from the summation of the wings of multiple nearby spectral lines. These lines produce time-dependent background signals that can dominate the uncertainty in measurement of absolute water vapor concentration. An example for water vapor in phosphine gas is given in Figure 7.17, acquired in the same experimental setup as that used for the spectra of water vapor in nitrogen illustrated in Figure 7.16. The absolute background has shifted upward relative to data in Figure 7.16 from nearby phosphine peak wings. Peaks from weak phosphine absorption lines are also visible within the range of the scan. The shift in the background due to slight changes in cavity pressure and temperature is readily apparent in Figure 7.17a. Although this background can be subtracted from the “wet” phosphine spectrum after realigning the spectra for optimal overlap of phosphine features, the resulting curve in Figure 7.17b contains more noise than does its counterpart in nitrogen matrix gas. The effect of background absorption by matrix gases encourages exploration for spectral windows that contain strong water vapor absorption lines but minimal matrix gas absorption, as has been shown for additional water vapor absorption lines in phosphine [95]. As the spectra move lower in energy toward more fundamental transitions, the water absorption peaks increase in strength, and matrix background peaks tend to be more isolated. As near- and mid-infrared laser and detector technologies improve, these spectral regions are likely to become more widely used in CRDS technology.

Another consideration in working with industrial gases is that many of them are reactive and corrosive. The reactions can both change the composition of impurities over time, either generating new water vapor from reactions between hydrides and

solid oxides in the gas cylinder wall, or consuming water and converting it to oxide particulates. Materials used in the construction of instrumentation must also be compatible with reactive gases. (Although a concern about mirror stability was raised early in the development of CRDS, modern dielectric mirrors have proven to be quite resistant to chemical attack by common semiconductor processing gases.) The uncertainties for water vapor concentration for corrosive gases are therefore higher than what can be obtained in inert matrices, and perhaps more significantly, depend on variable experimental conditions to a greater degree than identical measurements in inert matrices. The current state of the art for highly sensitive water vapor measurement in various industrial gases is summarized in Table 7.2. The column containing lower detectable limit (LDL) values should be interpreted somewhat loosely, as different authors applied different criteria for its determination. The units of this column are in parts per billion by volume ppbv, which is equivalent to nmol mol^{-1} in SI units.

Table 7.2 Performance for water vapor detection in various gases using CRDS^a

Matrix (Host Gas)	LDL (ppbv)	Comments	Ref.
Ammonia	10	Commercial instrument specification	[129]
Arsine	3.5		[127]
Chlorine	0.77	Assumes relative uncertainty in τ of 0.1 %	[90]
Hydrogen bromide	10	Estimated from stability of readings on gas with about 125 ppb concentration	[128]
	2.3	Assumes relative uncertainty in τ of 0.1 %	[90]
Hydrogen chloride	1.2	Assumes relative uncertainty in τ of 0.1 %	[90]
Nitrogen	2	Commercial instrument specification, instrument compatible with corrosives but no LDL specified	[130]
	0.44	Assumes relative uncertainty in τ of 0.1 %	[90]
	0.2	Commercial instrument specification	[131]
Oxygen	0.22	Assumes relative uncertainty in τ of 0.1 %	[90]
Phosphine	1.3	Absolute limit uncertain due to background absorption from phosphine	[126]
Silane	50	Corrected for dilution to 5 % silane in nitrogen to prevent particulate formation	[125]

^a See the text for a discussion of lower detectable limit (LDL) values.

7.4.4 Direct Frequency-Comb Spectroscopy

Direct frequency-comb spectroscopy (DFCS) is an optical detection technique that has been developed in recent years to address sensing challenges that cannot be

overcome by classical techniques such as TDLAS, CRDS, or FTIR spectroscopy. In particular, the combination of a broad spectral bandwidth with single-laser-line resolution and coherence is a unique detection capability for the DFCS technique, and it offers unprecedented potential for ultrasensitive, rapid multispecies detection for many experimental scenarios and applications [132–136].

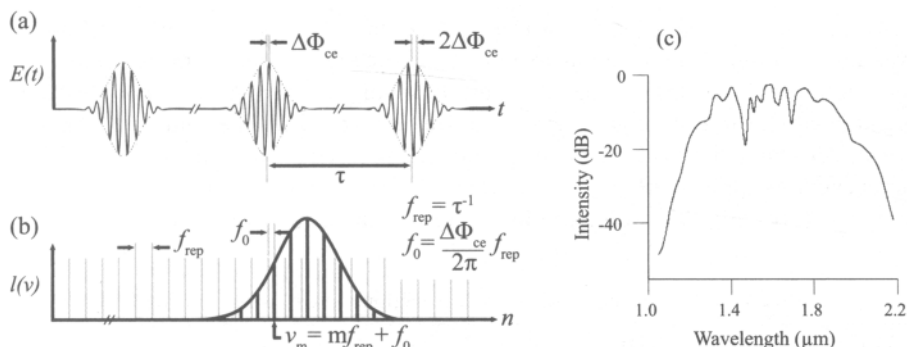


Figure 7.18 (a) Schematic time-domain picture of the pulse train of a mode-locked laser with the laser round-trip time τ and the carrier-envelope phase shift $\Delta\Phi_{ce}$. (b) Corresponding frequency-domain picture demonstrating the broadband comblike structure given by the laser repetition rate f_{rep} and the offset frequency f_0 . (c) Typical spectrum of an Er-doped fiber frequency comb broadened with a short piece of highly nonlinear fiber.

Properties of Frequency Combs Current frequency-comb sources are based almost entirely on mode-locked lasers. These systems were developed originally for their ultrafast pulse duration in the femtosecond or picosecond range. These pulses are emitted as an extremely regular train of pulses, resulting in a remarkably regular and stable frequency structure [137]. Figure 7.18a and b illustrate this connection: The short pulses in the time domain result in a very wide frequency spectrum according to the Fourier theorem; however, since the laser does not emit a single pulse but a train of pulses with extremely stable pulse-to-pulse period τ (given by the laser round-trip time), the spectrum becomes discretized and consists of a large number of narrow lines that are uniformly spaced by the laser repetition rate $f_{rep} = \tau^{-1}$. Resembling a comb in the frequency domain, this structure gives rise to the name “frequency comb.” Considering the underlying electric field in each ultrashort pulse emitted and the effect of dispersion usually present in the laser cavity, pulses are not exact copies of each other, but may experience phase shifts with respect to their intensity envelopes, known as carrier-envelope-phase (CEP) shift. Taking this effect into account in the frequency domain, we find a constant offset f_0 of the frequency comb from the exact integer multiples of f_{rep} . The optical frequency associated with every comb line can be defined exactly by only three parameters via $\nu_m = f_0 + mf_{rep}$, where m is an integer.

For DFCS the most commonly used frequency-comb sources are currently based on Er-doped fiber lasers [138–140]. These systems are commercially available, com-

pact, and easy to operate. Their near-infrared emission spectrum around $1.55\text{ }\mu\text{m}$ is a typical region for trace gas sensing and allows the use of many standard components from the telecommunications industry. The typical repetition rates range from 100 to 300 MHz. The direct spectrum emitted by Er-doped fiber mode-locked lasers covers the wavelength range from approximately 1.5 to $1.6\text{ }\mu\text{m}$ (or 6200 to 6700 cm^{-1} in wavenumbers), but may be extended further by using nonlinear optics for frequency conversion. Highly nonlinear fibers (HNFs) with extremely small core diameters allow a massive spectral broadening while preserving the comb's coherence properties. Figure 7.18c shows a typical spectrum of a Er-doped fiber laser broadened with a short piece (ca. 10 cm) of HNFs. At the -20-dB level relative to the spectral peak, the spectrum extends easily from 1.2 to $2.0\text{ }\mu\text{m}$, a span of more than 3300 cm^{-1} . With a repetition rate of 250 MHz for the comb used here, the spectrum contains approximately $400,000$ individual comb modes, each with a width of a few tens of kilohertz and an extremely well defined position ν_m given by $\nu_m = f_0 + mf_{\text{rep}}$. Furthermore, the position of each comb mode can be controlled precisely via f_0 and f_{rep} , and all lines can be used simultaneously, eliminating the need for wide and time-consuming frequency scans.

Coupling a Comb to an External Enhancement Cavity One of the biggest advantages of frequency combs compared to incoherent broadband light sources such as thermal emitters or fiber-based white-light supercontinua is the regular frequency-mode structure, which allows coupling the comb efficiently to high-finesse external enhancement cavities such as those used in CRDS. By matching the comb's repetition rate with the cavity's free spectral range (FSR) and adjusting the absolute frequency positions (via f_0), every comb line can be coupled exactly to a cavity mode, thereby allowing maximum coupling efficiency. The spectral bandwidth that can be coupled to the cavity, however, is usually smaller than the total bandwidth of the frequency comb, due to dispersion in the enhancement cavity. Mirror coatings and dispersion of any sample gas inside the cavity cause the cavity modes to be nonuniformly spaced. As a result, the comb and cavity modes slowly walk off perfect alignment away from the frequency, where the coupling is optimized. In general, the transmission bandwidth is limited to several tens of nanometers in the near infrared, corresponding to approximately 100 to 200 cm^{-1} . Of course, this bandwidth limit scales inversely with the cavity finesse. This restriction on the bandwidth transmitted simultaneously may be overcome by changing the lock point (frequency where transmission is optimized) or by dithering f_{rep} , which allows all comb lines to come on resonance with a cavity mode during one sweep of f_{rep} and results in transmission of the full comb spectrum when averaged over multiple dither cycles. A more detailed overview of comb-cavity coupling and an outline of various coupling schemes are provided by Thorpe, Adler, and others [135,136].

Cavity-enhanced direct frequency-comb spectroscopy (CE-DFCS) is an extremely powerful technique combining the sensitivity and resolution advantages of CW-CRDS with the broadband coverage of FTIR. Although earlier experiments were limited primarily by technical noise due to the more complicated broadband laser-cavity

coupling [122,141–143], quantum-limited detection sensitivity has been achieved recently for the first time in a CE–DFCS system [144].

Broadband, High-Resolution Detection Ideally, one would like to detect every single mode of the frequency-comb individually, to take advantage of the high spectral resolution and still cover simultaneously the entire bandwidth of the broadband comb. The vast difference in a frequency comb's mode spacing ($<0.01\text{ cm}^{-1}$) and its simultaneous bandwidth (hundreds of wavenumbers) is a significant challenge for many commonly used spectrographic tools, such as simple grating spectrographs; however, several approaches exist that are able to fulfill these requirements.

Figure 7.19 illustrates three of the most widely used spectrograph designs used in CE–DFCS. Figure 7.19a shows the VIPA spectrometer [122,133,141,142]. It is based on a tilted étalon plate, called a virtually imaged phased array (VIPA), which is able to provide very high angular dispersion (usually, oriented vertically). Since the VIPA is per design an étalon, the dispersion pattern is folded in every free spectral range (typically, $1.5\text{ to }3\text{ cm}^{-1}$). Therefore, a diffraction grating is used to unfold the overlapping VIPA orders in the horizontal plane, resulting in a two-dimensional diffraction pattern. The grating only has to resolve the coarsely spaced VIPA mode orders and is also able to image a wide bandwidth onto the two-dimensional detection array (typically, $200\text{ to }300\text{ cm}^{-1}$). The spectral resolution of a VIPA spectrometer is typically on the order of 0.03 cm^{-1} . Although this resolution is not sufficient to resolve individual lines of most frequency combs, it is virtually ideal for most experiments operating close to room temperature and atmospheric pressure, owing to molecular absorption linewidths on the order of 1 GHz (0.03 cm^{-1}). The two-dimensional spectrum on the camera provides a simultaneous broadband snapshot of all imaged comb lines and is therefore very useful for measuring fast processes [142]. By reading out the VIPA mode orders line by line, the two-dimensional spectrum is converted to a classical one-dimensional spectrum. If more detection bandwidth is required or if the laser wavelength does not allow the use of a VIPA, a Fourier transform spectrometer (FTS) may be used to detect the spectrum of a frequency comb. Figure 7.19b shows a typical setup with a scanning interferometer behind the comb and cavity [143,145,146]. The advantages of an FTS are its high detection bandwidth (usually larger than the comb bandwidth) and the fact that the resolution can easily be scaled via the length of the delay line. Therefore, an FTS can be designed to resolve single comb modes if necessary. Compared to an incoherent FTIR system, the disadvantage of limited throughput (étendue) at high spectral resolution vanishes when using a coherent light source such as a frequency comb; therefore, comb-FTS systems allow much faster data acquisition for high-resolution scans because of enhanced light transmission. A recently demonstrated system performs one scan at less than 0.01 cm^{-1} resolution in only a few seconds [144,146]. The interferometer also provides two signals with a relative phase shift, π , which allow using balanced detection to subtract technical noise from the comb-cavity coupling, resulting in shot-noise-limited sensitivity [144]. Despite its performance advantages, a scanning FTS has two drawbacks: Since it requires a mechanical delay, its size is quite substantial if high resolution is required, and the spectral information is collected over a time

frame of several seconds, ruling out the observation of dynamic processes. One method of speeding up the scan time of the FTS is dual-comb spectroscopy [147–149], which is illustrated in Figure 7.19c. Instead of a mechanical delay, a second frequency comb with a repetition rate that is slightly offset from the first comb is used to probe the light of the comb interacting with the sample. The small offset in f_{rep} mimics a fast scanning delay, as the pulse train from the second comb will evolve with respect to that of the first comb. A full scan (until the pulse from one laser overlaps again with a pulse from the other laser) can be performed in milliseconds or even microseconds, much faster than any mechanical delay; however, the spectral bandwidth, which can be scanned simultaneously without sample aliasing, decreases with faster sampling time [150]. Therefore, the right compromise will need to be found for a particular application. One further drawback of this method is also the need for two synchronized frequency combs. With compact and easily controllable Er:fiber systems, the additional laser is manageable; however, with more complex systems such as the ones used for mid-infrared spectroscopy [146], the dual-comb setup becomes rather complex.

Experimental Demonstration of Trace Water Detection in Arsine Recently, frequency-comb-based detection of impurities in specialty gases was demonstrated for the first time. In particular, the experiment showed ultrasensitive detection of trace water vapor in the semiconductor gas arsine [122]. The spectral band selected was a rarely explored window of transmission in arsine around 5500 res. The employed frequency comb was an Er:fiber system that was spectrally broadened with a piece of HNF, yielding the spectrum shown in Figure 7.18c. The remaining setup is similar to the one shown in Figure 7.19a, using an enhancement cavity with a finesse of 30,000 and a VIPA spectrometer with a resolution of 0.03 cm^{-1} . The high-finesse cavity contained the sample gas (arsine + trace water vapor). For data normalization, we also collected reference spectra when we replaced the sample gas with dry nitrogen. The sample absorption obtained is depicted in Figure 7.20 and clearly highlights the major advantage of the broadband and high-resolution CE–DFCS technique. Although the entire spectrum is dominated by densely spaced arsine absorption features, water absorption lines are clearly identified (using known positions from the HITRAN spectroscopic database [96]), such as those seen in the magnified inset. The spectrum collected contains dozens of water lines and hence enables a very precise and sensitive measurement of the water concentration. Here, the concentration of trace water was determined to be 310 ppbv with a minimum detectable concentration of 31 ppbv.

As a first demonstration of using CE–DFCS for this type of experiment, the results presented here still have a large room for improvement. For instance, the total covered spectral bandwidth of the CE–DFCS system was 5000 to 5800 cm^{-1} . Thus, the system was able to cover the absorption bands of multiple additional important impurity species, such as methane, hydrogen sulfide, carbon dioxide, or silane (demonstrated by using nitrogen as carrier gas instead of arsine). Only the limited transparency of arsine in the chosen spectral window restricted the trace detection to water. It is likely that different spectral windows and/or different specialty

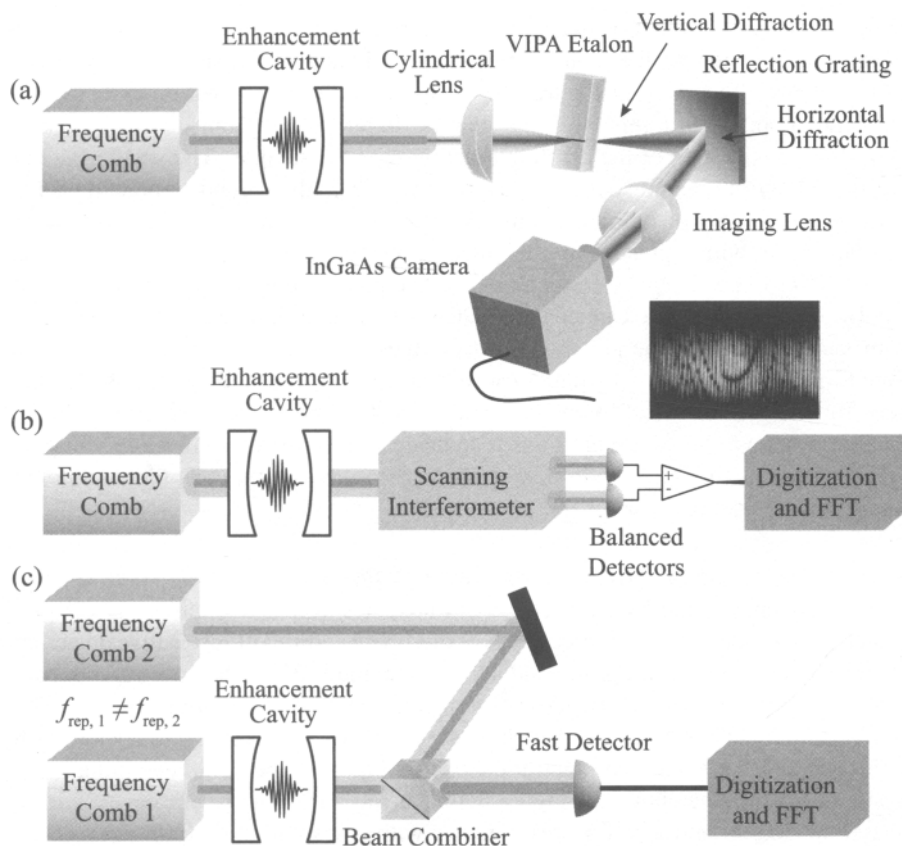


Figure 7.19 Detection schemes for cavity-enhanced direct frequency-comb spectroscopy: (a) VIPA spectrometer, (b) Fourier transform spectroscopy with a mechanically scanning interferometer, and (c) dual-comb spectroscopy using two synchronized mode-locked lasers.

gases (e.g., phosphine or silane) will allow the comb system to demonstrate its full potential more effectively. In addition, technical noise provided a major limitation to the sensitivity; recent efforts in overcoming technical noises have resulted in dramatic improvements of the sensitivity, reaching the shot-noise limit and promising much lower detection limits for future experiments [144]. An optimized CE-DFCS system is probably capable of achieving sub-ppbv detection sensitivity for trace water impurity.

Extension of Comb Spectroscopy into the Mid-infrared One particular advantage of frequency combs, which is already used in the HNF-based spectral broadening, is the fact that nonlinear optics can be exploited to access spectral regions that are not covered directly by the laser system. One example is the extension of frequency-comb technology into the mid-infrared, where the fundamental vibra-

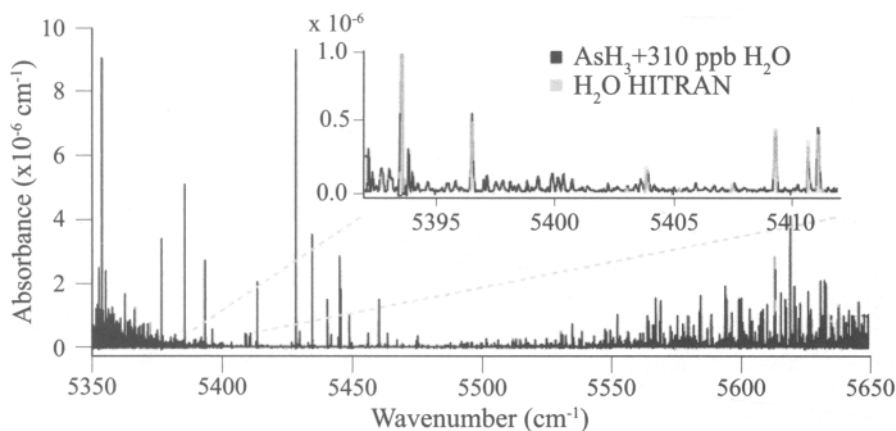


Figure 7.20 Spectrum of arsine gas around 5500 cm^{-1} with trace quantities of water vapor (310 ppbv). The inset shows the positions of the water lines taken from the HITRAN database.

tional absorption bands of typical trace molecules are located. These bands can be significantly stronger than that of their near-infrared overtones. In the case of water, the fundamental O–H stretch vibration band around 3700 cm^{-1} is approximately 10 times stronger than the band around 5350 cm^{-1} , which was used in the previously described experiment [96]. Other species offer even larger gains in line strength (e.g., 100 for methane and even 10^4 for carbon dioxide).

The first fully operable frequency-comb spectroscopy system in the molecular fingerprint region (frequencies below 4000 cm^{-1}) was demonstrated recently. Using a high-power Yb: fiber laser (fundamental operating wavelength at $1.05\text{ }\mu\text{m}$) to pump an optical parametric oscillator synchronously [151], the frequency-comb source provides a tunable output ranging from center wavelengths of 2.8 to $4.8\text{ }\mu\text{m}$ (corresponding to approximately 3600 to 2100 cm^{-1}) with a simultaneous spectral bandwidth of up to 300 cm^{-1} [146]. The entire spectroscopy setup is similar to Figure 7.19b, with a scanning Michelson interferometer for Fourier transform spectroscopy and a Herriott multipass cell instead of the enhancement cavity. Although the multipass cell provides only a total increased pathlength of 36.4 m compared to many kilometers of enhanced pathlength possible with an optical cavity, the access to strong absorption features in the mid-infrared still resulted in extremely low detection limits, to below the ppbv level. To implement cavity enhancement in this spectral region, high-quality low-dispersion mirrors will be needed; however, this requirement still presents a challenge for current optical coating technology. Figure 7.21 shows a collection of demonstration spectra collected with this mid-infrared comb Fourier transform spectroscopy system. Figures 7.21a and b show that the system's capability of covering a wide spectral window enables the detection and quantification of both species with a clear line spectrum such as methane and molecules with wide, continuous absorption features such as isoprene. At the same time, the system also offers high resolution as demonstrated in Figure 7.21c, which shows a magnified

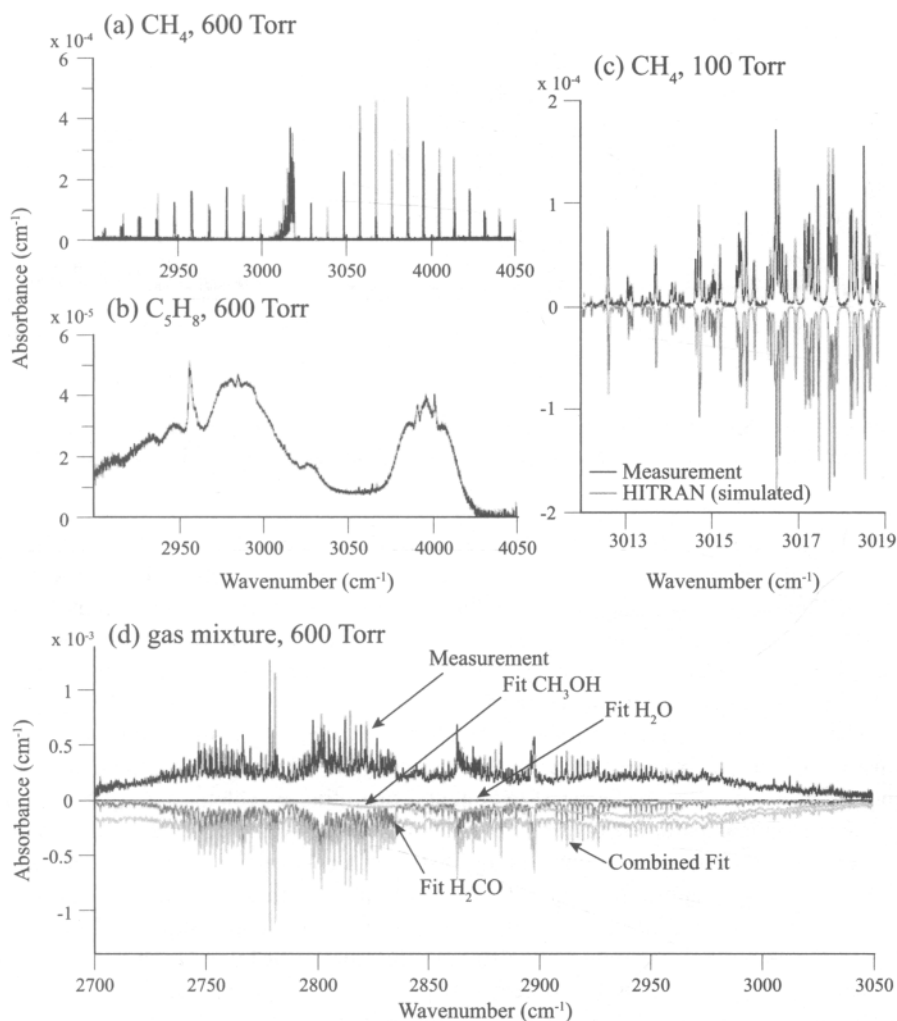


Figure 7.21 Typical spectra collected with a mid-infrared frequency-comb Fourier transform spectrometer: (a) spectrum of 10 ppmv methane in 600 torr (80 kPa) of nitrogen in the fundamental C–H-stretch spectral window around 3000 cm^{-1} at a resolution of 0.0056 cm^{-1} , (b) spectrum of 16 ppmv of isoprene in 600 torr (80 kPa) of nitrogen at a resolution of 0.058 cm^{-1} , (c) magnified view of the methane Q-branch to highlight the resolution of the mid-infrared comb-FTS (data in black above, HITRAN fit in gray below), and (d) spectrum of a mixture of formaldehyde, methanol, and water in 600 torr (80 kPa) of nitrogen (black) and the numerical concentration fits below based on spectral reference data for formaldehyde, methanol, water, and the combined fit.

view of the methane Q-branch. Finally, a combination of the comb-FTS's high resolution and wide bandwidth is utilized by quantifying a mixture of gases, as shown in Figure 7.21d. Here, the sample contains formaldehyde, methanol, and water. A simple fitting algorithm and a database with the molecules' reference spectra extract precise concentrations for the constituents, in this case, 47.1 ppmv of formaldehyde, 58.3 ppmv of methanol, and 813 ppmv of water in 600 torr (80 kPa) of nitrogen. The precision attained depends on the number of absorption features present for each molecule, but the concentration determined for methanol is particularly impressive. Whereas the continuous absorption background of methanol would impose a major challenge for any CW laser technique, the frequency-comb system is able to determine the concentration of methanol in this sample with a relative precision of 0.07 %.

Despite a variety of powerful demonstrations over the last few years, frequency-comb spectroscopy is still a technique under development. Current efforts focus on the generation of more stable, more broadband, and longer-wave mid-infrared combs, as well as novel ideas focusing on overcoming noise limitations to push for better sensitivity. Considering their unique capabilities, frequency combs will certainly play a major role in future trace detection applications.

7.5 Conclusions

Development of analytical methods for the measurement of water vapor impurity in inert and specialty gases is especially important in the manufacture of microelectronic devices that continue to decrease in size and become increasingly more complex. The need to control water vapor at trace levels in a range of gases used in critical process steps requires not only rapid, reliable, and selective gas-phase measurement but also high-sensitivity approaches. In the last decade many advances in the development and application of sensor and laser absorption spectroscopic techniques have taken place, and hence this chapter has focused primarily on these areas. Existing sensor technologies continue to be refined, and new sensor materials and approaches are being actively investigated. Even more significant is the rapid development of near-infrared laser spectroscopic methods using long-path cells and enhancement cavities, opening up new capabilities for the trace analytical chemist. Methods such as CRDS and TDLAS now enable high-sensitivity water vapor measurements down to 100 to 200 pptv in inert gas matrices in small, easy-to-use, relatively low-cost instrumentation. Just 10 years ago, such sensitivities were attainable only with much more expensive and complex research equipment (e.g., APIMS).

In the future we envisage advances in laser spectroscopic techniques continuing along the same path but extending into the mid-infrared region, as efficient and cost-effective mid-infrared laser sources become more widely available. These methods will offer enhanced sensitivity over current methods by making use of more intense fundamental absorption lines rather than less intense overtone or combination lines. Furthermore, in some cases the methods will widen the spectroscopic region available, enabling simultaneous detection of water vapor and other gas-phase impurities. CE-

DFCS is one such technique that shows considerable potential in this regard. Other emerging mid-infrared laser absorption spectroscopic techniques (some of which are described and discussed in Chapter 4) will probably also be developed specifically for moisture analysis. However, as already emphasized in this chapter, the successful application of any new spectroscopic method in multiple gas matrices will still depend on being able to locate a transmission window where strong analyte absorption lines can be accessed cleanly.

REFERENCES

1. Funke, H. H., Grissom, B. L., McGrew, C. E., & Raynor, M. W. (2003). Techniques for the measurement of trace moisture in high-purity electronic specialty gases. *Review of Scientific Instruments*, 74, 9, 3909–3933.
2. Monroe, S. (1998). Trace moisture in ammonia: Gas chromatography using calcium carbide. *Journal of the Institute of Environmental Sciences and Technology*, 41, 1, 21–25.
3. Siefert, K., Berger H., & Whitlock, W. (1993). Quantitative analysis of contaminants in ultrapure gases at the parts per trillion level using atmospheric pressure ionization mass spectroscopy. *Journal of Vacuum Science Technology A*, 11, 1593–1597.
4. Ketkar S., & Dheandhanoo, S. (2001). Use of ion mobility spectrometry to determine low levels of impurities in gases. *Analytical Chemistry*, 73, 2554–2557.
5. Ketkar, S., Dheandhanoo, S., & Scott, A. (2004). Comparison of APIMS and IMS for the analysis of trace impurities in inert gases. *SEMI Technology Symposium: Innovations in Semiconductor Manufacturing, Semicon West 2004, San Francisco, CA*, pp. 89–108.
6. Warrick, B. (2004). Detection of gas phase impurities: a comparison of API-MS and IMS technologies. *SEMI Technical Symposium (STS): Innovations in Semiconductor Manufacturing*. San Jose, CA: Semiconductor Equipment and Materials International, pp. 109–129
7. Bandy, A. R., Tu, F. H., Mitchell, G. M., & Ridgeway, R. G. (2002). Determination of moisture in anhydrous ammonia at the ppbv level using negative ion APIMS. *Proceedings of SEMICON West 2002, SEMI Technical Symposium: Innovations in Semiconductor Manufacturing, San Francisco, CA*, pp. 163–170.
8. Okhi A., Ohmi, T., Date, J., & Kijima T. (1998). Highly purified silane gas for silicon semiconductor devices. *Journal of the Electrochemical Society*, 145, 3560–3569.
9. Kitano, M., Shirai, Y., Ohki, A., Babasaki, S., & Ohmi, T. (2001). Impurity measurement in specialty gases using an atmospheric pressure ionization mass spectrometer with a two compartment ion source. *Japanese Journal of Applied Physics*, 40, 2688–2693.
10. Ma, C., Athalye, A., Fruhberger, B., & Ezell, E. (1998). Moisture dry-down in high purity hydrogen chloride. *Proceedings of Contamination Control, Phoenix, AZ*. Mount Prospect, IL: Institute of Environmental Sciences and Technology, pp. 285–289.
11. Meyer, C. W., Hodges, J. T., Hyland, R. W., Scace, G. E., Valencia-Rodriguez, J., & Whetstone, J. R. (2010). The second-generation NIST standard hygrometer. *Metrologia*, 47, 192–207.

12. Meyer, C. W., Hodges, J. T., Huang, P. H., Miller, W. W., Ripple, D. C., & Scace, G. E. (2008). *Calibration of Hygrometers with the Hybrid Humidity Generator*. NIST Special Publication 250-83. Washington, DC: USDOC and NIST.
13. Scace, G. E., Huang, P. H., Hodges, J. T., Olson, D. A., & Whetstone, J. R. (1997). The new NIST low frost-point humidity generator. *Proceedings of the 1997 National Conference of Standards Laboratories Workshop and Symposium*. Boulder, CO: NCSL International.
14. Scace, G. E., & Hodges, J. T. (2002). Uncertainty of the NIST low frost-point humidity generator. In B. Fellmuth, J. Seidel, and G. Scholz (Eds.), *Proceedings of TEMPMEKO 2001: Eighth International Symposium on Temperature and Thermal Measurements in Industry and Science*. Berlin: VDE Verlag, pp. 597–602.
15. Hodges, J. T., & Scace, G. E. (2006). Developing advanced humidity standards to measure trace water vapor in specialty gases. *MICRO*, 24, 59.
16. Ketkar, S. N., Scott, A. D., Jr., & Martinez de Pinillos, J. V. (1994). Dynamic dilution calibration system for calibrating analytical instruments used in gas analysis. *Journal of the Electrochemical Society*, 141, 1, 184–187.
17. McAndrew, J. J. F. (1997). Humidity measurement in gases for semiconductor processing. In J. D. Hogan (Ed.), *Specialty Gas Analysis: A Practical Guidebook*. New York: Wiley VCH, pp. 21–42.
18. Wiederhold, P. R. (2000). The principles of chilled mirror hygrometry. *Sensors*, 17, 7, 46–51.
19. Keidel, F. A. (1959). Determination of water by direct amperometric measurement. *Analytical Chemistry*, 31, 12, 2043–2048.
20. Zatko, D. A., & Maguire, J. F. (1989). *Low level moisture measurement system and method*. U.S. Patent No. 4,800,000. Washington, DC: U.S. Patent and Trademark Office.
21. Ma, C., Shadman, F., Mettes, J., & Silverman, L. (1995). Evaluating the trace-moisture measurement capability of coulometric hygrometry *MICRO*, 13, 4, 43–49.
22. Bell, S. A., Gardiner, T., Gee, R. M., Stevens, M., Waterfield, K., & Woolley, A. (2004). An evaluation of performance of trace moisture measurement methods. *Proceedings of 9th International Symposium on Temperature and Thermal Measurements in Industry and Science*, 1, 663–668.
23. Manickum, V., Prabhu, E., Jayaraman, V., Gnanasekar, K. I., Gnanasekaran, T., & Nagaraja, K. S. (2010). Electrolytic sensor for trace level determination of moisture in gas streams. *Measurement*, 43, 10, 1636–1643.
24. Wiederhold, P. R. (1997). *Water Vapor Measurement Methods and Instrumentation*. New York: Marcel Dekker.
25. Capuano, I. A., & Mathieu, R. J. (1999). A rapid response electrolytic amperometric moisture analyzer. *American Laboratory*, 31, 30–33.
26. Sauerbrey, G. Z. (1959). Use of quartz vibrator for weighing thin films. *Zeitschrift für Physik*, 155, 206–212.
27. O'Sullivan, C. K., & Guilbault, G. G. (1999). Commercial quartz crystal microbalances: theory and applications. *Biosensors and Bioelectronics*, 14, 8/9, 663–670.
28. Blakemore, C. B. (1985). Piezoelectric moisture analyzer for semiconductor gases. In K. Herbst (Ed.), *Proceedings of the 31st Annual ISA Analysis Division Symposium*, Vol. 21. Research Triangle Park, NC: Instrument Society of America, p. 125.

29. Kleinfeld, E. R., & Ferguson, G. S. (1995). Rapid, reversible sorption of water from the vapor by a multilayered composite film: a nanostructured humidity sensor. *Chemical Materials*, 7, 2327–2331.
30. Halper, S. R., & Villahermosa R. M. (2009). Cobalt-containing polyimides for moisture sensing and absorption. *ACS Applied Material Interfaces*, 1, 5, 1041–1044.
31. Bear, R. S., Jr., & Hauer, R. (2002). Designing a ppb class moisture analyzer: evolution and technical hurdles. *Standards Workshop on New Advances in Detection of Trace (< 1 ppb) Impurities in Bulk Inert Gases, SEMICON West 2002, July 23, San Francisco, CA*.
32. Feng, J., & Raynor, M. W. (2007). Trace water vapor detection in pure arsine gas using quartz crystal oscillator technology. *Pittsburgh Conference on Analytical Chemistry and Applied Spectroscopy (Pittcon), Chicago, February 25–March 2*.
33. Wei, J., Pillion, J. E., & Hoang, C. (1997). In-line moisture monitoring in semiconductor process gases by a reactive metal coated quartz crystal microbalance. *Journal of the Institute of Environmental Sciences and Technology*, 40, 43–48.
34. Wei, J., Pillion, J. E., King, M., & Verlinden, M. (1997). Using an in-line monitor to obtain real-time moisture measurements. *MICRO*, 15, 31–36.
35. Toth, M. I., Zatko, D. A., Yesenofski, D. F., Schneegans, M., & Helneder, J. (1997). Beta testing an in-line monitor for moisture measurement in inert gas lines. *MICRO, July/August*, 79–92.
36. Huang, P. H. (1998). Humidity standards for low level water vapor sensing and measurement. *Sensors and Actuators B*, 53, 1, 125–127.
37. Beaubien, D. J. (2005). The chilled mirror hygrometer: how it works, where it works and where it doesn't. *Sensors*, 22, 5, 30–34.
38. Flaherty, E., Herold, C., Murray, D., & Thompson, S. R. (1986). Determination of water in hydrogen chloride gas by condensation technique. *Analytical Chemistry*, 58, 1903–1904.
39. Chen, Z., & Lu, C. (2005). Humidity sensors: a review of materials and mechanisms. *Sensor Letters*, 3, 274–295.
40. Hasagawa, S. (1980). Performance characteristics of a thin film aluminum oxide humidity sensor. *Proceedings of the 30th Electronic Components Conference, San Francisco, CA*. New York: IEEE, pp. 386–391.
41. Mehrhoff, T. K. (1985). Comparison of continuous moisture monitors in the range 1 to 15 ppm. *Review of Scientific Instruments*, 56, 1930–1933.
42. Nahar, R. K. (2002). Physical understanding of moisture induced degradation of non-porous aluminum oxide thin films. *Journal of Vacuum Technology B*, 20, 382–385.
43. Clevett, K. J. (1986). *Process Analyzer Technology*. New York: John Wiley & Sons.
44. Kerney, J. (2007). New method for trace moisture measurement. *Advances in Wafer Processing Session, SEMICON West, San Francisco, CA*.
45. Feng, J., & Raynor, M. W. (2009). Trace water vapor analysis under 100 ppb using cavity ring-down, oscillating quartz crystal and electrical impedance technologies. *Specialty Gas Session, Pittsburgh Conference on Analytical Chemistry and Applied Spectroscopy (Pittcon), Chicago, February 25–March 2*.

46. Coates, J. (1998). Vibrational spectroscopy: instrumentation for infrared and Raman spectroscopy. *Applied Spectroscopy Reviews*, 33, 4, 267–425.
47. Griffith, P. R., & de Haseth, J. A. (2007). *Fourier Transform Infrared Spectroscopy*. Hoboken, NJ: John Wiley & Sons.
48. Smith, B. C. (2011). *Fundamentals of Fourier Transform Infrared Spectroscopy*, 2nd ed. Boca Raton, FL: CRC Press.
49. Saptari, V. (2004). Fourier-transform spectroscopy instrumentation engineering. In *SPIE Tutorial Texts in Optical Engineering*, Vol. TT61. Bellingham, WA: Society for Photo-optical Instrumentation Engineers.
50. Kinch, M. A. (2007). *Fundamentals of Infrared Detector Materials*. Bellingham, WA: SPIE, The Society for Photo-optical Instrumentation Engineers.
51. Rogalski, A. (2011). *Infrared Detectors*, 2nd ed. Boca Raton, FL: CRC Press.
52. Richardson, R. L., Yang, H., & Griffiths, P. R. (1998). Evaluation of a correction for photometric errors in FT-IR spectrometry introduced by a non linear detector response. *Applied Spectroscopy*, 52, 4, 565–571.
53. White, J. U. (1942). Long optical paths of large aperture. *Journal of the Optical Society of America*, 32, 5, 285–285.
54. Vahey, P. G., Meyer, R. T., & Perez, J. E. (2006). Overcoming hydrogen bonding in on-line FTIR spectroscopy of hydrofluoric acid. *Gases and Technology*, 5, 1, 18–22.
55. Millward, A., Davia, D., Wyse, C., Seymour, A., Vininski, J., Torres, R., & Raynor, M. (2009). *Anhydrous Hydrogen Fluoride for Selective Etch Processes: Measurement and Control of Water and Metallic Impurities*. Taiyo Nippon Sanso Corporation Technical Report 28, pp. 17–22.
56. Stallard, B. R., Rowe, R. K., Garcia, M. J., Haaland, D. M., Espinoza, L. H., & Niemczyk, T. M. (1993). *Trace Water Vapor Determination in Corrosive Gases by Infrared Spectroscopy*. Sandia National Laboratories Report SAND 93-4026 UC-411.
57. Espinoza, L. H., Niemczyk, T. M., Stallard, B. R., & Garcia, M. J. (1997). *Trace Water Vapor Determination in Nitrogen and Corrosive Gases using Infrared Spectroscopy*. Sandia National Laboratories Report SAND 97-1494 UC-411.
58. Stallard, B. R., Espinoza, L. H., & Niemczyk, T. M. (1995). Trace water vapor determination in gases by infrared spectroscopy. *Proceedings of the 41st Annual Technical Meeting of the Institute of Environmental Sciences, Anaheim, CA*, pp. 1–8.
59. Stallard, B. R., Espinoza, L. H., Rowe, R. K., Garcia, M. J., & Niemczyk, T. M. (1995). Trace water vapor detection in nitrogen and corrosive gases by FTIR spectroscopy. *Journal of the Electrochemical Society*, 142, 8, 2777–2782.
60. Espinoza, L. H., Niemczyk, T. M., & Stallard, B. R. (1998). Generation of synthetic background spectra by filtering the sample interferogram in FT-IR. *Applied Spectroscopy*, 52, 3, 375–379.
61. Nishikida, K., Nishio, E., & Hannah, R. W. (1995). *Selected Applications of Modern FTIR Techniques*. Tokyo: Kodansha.
62. Jaakkola, P., Tate, J. D., Paakkunainen, M., Kauppinen, J., & Saarinen, P. (1997). Instrumental resolution considerations for Fourier transform infrared gas-phase spectroscopy. *Applied Spectroscopy*, 51, 8, 1159–1169.

63. Anderson, R. J., & Griffiths, P. R. (1975). Errors in absorbance measurements in infrared transform spectrometry because of limited instrument resolution. *Analytical Chemistry*, 47, 14, 2339–2347.
64. Pivonka, D. E. (1991). The infrared spectroscopic determination of moisture in HCl for the characterization of HCl gas drying resin performance. *Applied Spectroscopy*, 45, 4, 597–603.
65. Salim, S., Litwin, M. M., & Natwora, J. P. J. (1998). FTIR spectroscopy for measurement of moisture levels in hydride and corrosive gases. Workshop on Gas Distribution Systems, *Proceedings of SEMICON West 1998, San Francisco, CA*, pp. D1–D18.
66. Miyazaki, K., & Kimura, T. (1993). Analysis of trace impurities in corrosive gases by gas-phase FTIR. *Bulletin of the Chemical Society of Japan*, 66, 11, 3508–3510.
67. Salim, S., & Gupta, A. (1996). Measurement of trace levels of moisture in UHP hydride gases by Fourier transform infrared spectroscopy. *Proceedings of CleanRooms 1996 West Session 602, Santa Clara, CA*, 22, 22–32.
68. Mitchell, G. M., Vorsa, V., Ryals, G. L., Milanowicz, J. A., Ragsdale, D. J. M., Marhefka, K. L., Wagner, M., & Ketkar, S. N. (2002). Trace impurity detection in ammonia for the compound semiconductor market. SEMI Technical Symposium: Innovations in Semiconductor Manufacturing. *Proceedings of SEMICON West 2002, San Francisco, CA*, p. 199.
69. Funke, H. H., Raynor, M. W., Yucelen, B., & Houlding, V. H. (2001). Impurities in hydride gases: 1. Investigation of trace moisture in the liquid and vapor phase of ultra-pure ammonia by FTIR spectroscopy. *Journal of Electronic Materials*, 30, 11, 1438–1447.
70. Yao, J., Funke, H. H., & Raynor, M. (2004). Spectroscopic methods for trace moisture detection in electronic specialty gases. *Nippon Sanso Corporation Engineering Report*, 23, 43–49.
71. Haaland, D. M. (1992). Multivariate calibration methods applied to quantitative analysis of infrared spectra. P. C. Jurs (Ed.), *Computer-Enhanced Analytical Spectroscopy*, Vol. 3. New York: Plenum Press, pp. 1–30.
72. Haaland, D. M., & Easterling, R. G. (1980). Improved sensitivity of infrared spectroscopy by the application of least squares methods. *Applied Spectroscopy*, 34, 5, 539–548.
73. Haaland, D. M., & Thomas, E. V. (1988). Partial least-square methods for spectral analysis. *Analytical Chemistry*, 60, 1193–1202.
74. Hovde, D. C., Hodges, J. T., Scace, G. E., & Silver, J. A. (2001). Wavelength-modulation laser hygrometry for ultrasensitive detection of water vapor in semiconductor gases. *Applied Optics*, 40, 6, 829–839.
75. Wu, S. Q., Morishita, J., Masusaki, H., & Kimishima, T. (1998). Quantitative analysis of trace moisture in N₂ and NH₃ gases with dual-cell near infrared diode laser absorption spectroscopy. *Analytical Chemistry*, 70, 15, 3315–3321.
76. Wu, S. Q., Masusaki, H., Ishihara, Y., Matsumoto, K., Kimishima, T., Morishita, J., Kuze, H., & Takeuchi, N. (1996). Trace moisture measurements with dual beam diode laser spectroscopy. *Proceedings of the 5th International Symposium on Semiconductor Manufacturing*. Piscataway, NJ: Institute of Electrical and Electronics Engineers, pp. 321–324.

77. Kermarric, O., Campidelli, Y., Bensahel, D., Ly, C. H., & Mauvais, P. (2002). The detrimental effect of moisture in SiGe epitaxy. *Solid State Technology*, 45, 55–60.
78. Wright, A. O., Wood, C. D., Reynolds K. J., & Malczewski, M. L. (2004). Detecting single digit part-per-billion levels of moisture in ammonia gas. *MICRO*, 22, 47–55.
79. Inman, R. S., & McAndrew, J. J. F. (1994). Application of tunable diode laser absorption spectroscopy to trace moisture measurements in gases. *Analytical Chemistry*, 66, 2471–2479.
80. Funke, H. H., Yao, J., Raynor M. W., & Wright A. O. (2004). Using tunable diode laser spectroscopy to detect trace moisture in ammonia. *Solid State Technology*, 47, 10, 49–54.
81. McAndrew, J., Bartolomey, M., Girard, J. M., Goltz, G., & Flan, J. M. (2000). Implementing on-line and in-situ moisture monitoring in reactive gas environments. *MICRO*, 18, 39–47.
82. Vorsa, V., Dheandhanoo, S., Yesenofski, D., & Wagner, M. (2003). Measuring moisture in corrosive gases using TDLAS and CRDS. *Workshop on Advances in Detection of Trace Moisture in Specialty Gases, Semicon West 2003, July 14, San Francisco, CA*.
83. McAndrew, J. (1998). Progress in in-situ contamination control. *Semiconductor International*, 21, 71–78.
84. Bomse, D. S., Stanton, A. C., & Silver, J. A. (1992). Frequency modulation and wavelength spectroscopies: comparison of experimental methods using lead-salt diode laser. *Applied Optics*, 31, 718–731.
85. Silver, J. A. (1992). Frequency modulation spectroscopy for trace species detection: theory and comparison of among experimental methods. *Applied Optics*, 31, 707–717.
86. Reid, J., & Labrie, D. (1981). Second harmonic detection with tunable diode lasers: comparison of experiment and theory. *Applied Physics B*, 26, 203–210.
87. Feher, M., & Martin, P. A. (1995). Review: tunable diode laser monitoring of atmospheric trace gas constituents. *Spectrochimica Acta A*, 51, 1579–1599.
88. Lisak, D., Hodges, J. T., & Ciurylo, R. (2006). Comparison of semiclassical line-shape models to rovibrational H₂O spectra measured by frequency-stabilized cavity ring-down spectroscopy. *Physical Review A*, 73, 012507.
89. Tran, H., Bermejo, D., Domenech, J. L., Joubert, P., Gamache, R. P., & Hartmann, J. M. (2007). Collisional parameters of H₂O lines: velocity effects on the line shape. *Journal of Quantitative Spectroscopy and Radiative Transfer*, 108, 1, 126–145.
90. Vorsa, V., Dheandhanoo, S., Ketkar, S. N., & Hodges, J. T. (2005). Quantitative absorption spectroscopy of residual water vapor in high-purity gases: pressure broadening of the 1.392,53 μm H₂O transition by N₂, HCl, HBr, Cl₂, and O₂. *Applied Optics*, 44, 4, 611–619.
91. Amerov, A., Maskas, M., Meyer, W., Fiore, R., & Tran, K. (2007). New process gas analyzer for the measurement of water vapor concentration. *Proceedings of Instrumentation, Systems and Automation Society 52nd Analysis Division Symposium, Houston, TX, April 15–10*, pp. 63–74.
92. Soleyn, K. (2009). Development of tunable diode laser absorption spectroscopy moisture analyzer for natural gas. *Proceedings of 5th International Gas Analysis Symposium and Exhibition, Rotterdam, The Netherlands, February 11–13*.

93. Dean, W. (2006). In-situ analysis of trace moisture in chlorine gas streams using a tunable diode laser. *Proceedings of the Instrumentation, Systems and Automation Society 51st Analysis Division Symposium, Anaheim, CA, April 2–6*, pp. 1–8.
94. Lackner, M. (2007). Tunable diode laser absorption spectroscopy (TDLAS) in the process industries: a review. *Chemical Engineering*, 23, 2, 65–147.
95. Lehman, S. Y., Bertness, K. A., & Hodges, J. T. (2004). Optimal spectral region for real-time monitoring of sub-ppm levels of water in phosphine by cavity ring-down spectroscopy. *Journal of Crystal Growth*, 261, 2/3, 225–230.
96. Rothman, L. S., Gordon, I. E., Barbe, A., Benner, D. C., Bernath, P. E., Birk, M., Boudon, V., et al. (2009). The HITRAN 2008 molecular spectroscopic database. *Journal of Quantitative Spectroscopy and Radiative Transfer*, 110, 533–572.
97. Lisak, D., Havey, D. K., & Hodges, J. T. (2009). Spectroscopic line parameters of water vapor for rotation–vibration transitions near 7180 cm^{-1} . *Physical Review A*, 79, 052507.
98. Lisak, D., & Hodges, J. T. (2008). Low-uncertainty H_2O line intensities for the 930-nm region. *Journal of Molecular Spectroscopy*, 249, 1, 6–13.
99. Aarts, I. M. P., Pipino, A. C. R., de Sanden, M., & Kessels, W. M. M. (2007). Absolute in-situ measurement of surface dangling bonds during a-Si:H growth. *Applied Physics Letters*, 90, 16.
100. Johnston, P. S., & Lehmann, K. K. (2008). Cavity enhanced absorption spectroscopy using a broadband prism cavity and a supercontinuum source. *Optics Express*, 16, 19, 15013–15023.
101. Busch, K. W., Hennequin, A., & Busch, M. A. (1999). Mode formation in optical cavities. In K. W. Busch and M. A. Busch (Eds.), *Cavity-Ringdown Spectroscopy an Ultratrace-Absorption Measurement Technique*. Washington, DC: American Chemical Society, pp. 7–48.
102. Anderson, D. Z., Frisch, J. C., & Masser, C. S. (1984). Mirror reflectivity based on optical cavity decay. *Applied Optics*, 23, 1238–1245.
103. Hodges, J. T., & Ciurylo, R. (2005). Automated high-resolution frequency-stabilized cavity ring-down absorption spectrometer. *Review of Scientific Instruments*, 76, 2, 023112.
104. Fox, R. W., & Hollberg, L. (2002). Role of spurious reflections in ring-down spectroscopy. *Optics Letters*, 27, 20, 1833–1835.
105. Paldus, B. A., Harb, C. C., Spence, T. G., Zare, R. N., Gmachl, C., Capasso, F., Sivco, D. L., et al. (2000). Cavity ringdown spectroscopy using mid-infrared quantum-cascade lasers. *Optics Letters*, 25, 9, 666–668.
106. Brumfield, B. E., Steward, J. T., Weaver, S. L. W., Escarra, M. D., Howard, S. S., Gmachl, C. F., & McCall, B. J. (2010). A quantum cascade laser CW cavity ringdown spectrometer coupled to a supersonic expansion source. *Review of Scientific Instruments*, 81, 6, 063102.
107. Tan, Z., Long, X., Yuan, J., Huang, Y., & Zhang, B. (2009). Precise wavelength calibration in continuous-wave cavity ringdown spectroscopy based on the HITRAN database. *Applied Optics*, 48, 12, 2344–2349.
108. van Zee, R. D., Hodges, J. T., & Looney, J. P. (1999). Pulsed, single-mode cavity ringdown spectroscopy. *Applied Optics*, 38, 18, 3951–3960.

109. Looney, J. P., Hodges, J. T., & van Zee, R. D. (1999). Quantitative absorption measurements using cavity ringdown spectroscopy with pulsed lasers. In K. W. Busch and M. A. Busch (Eds.), *Cavity-ringdown spectroscopy an ultratrace-absorption measurement technique*. Washington, DC: American Chemical Society, pp. 93–105.
110. Ye, J., Ma, L. S., & Hall, J. L. (1999). Using FM methods with molecules in a high finesse cavity: A demonstrated path to $<10^{-12}$ absorption sensitivity. In K. W. Busch and M. A. Busch (Eds.), *Cavity-Ringdown Spectroscopy an Ultratrace-Absorption Measurement Technique*. Washington, DC: American Chemical Society, pp. 233–257.
111. Huang, H., & Lehmann, K. K. (2008). CW cavity ring-down spectroscopy (CRDS) with a semiconductor optical amplifier as intensity modulator. *Chemical Physics Letters*, 463, 246–250.
112. Drever, R. W. P., Hall, J. L., Kowalski, F. V., Hough, J., Ford, G. M., Munley, A. J., & Ward, H. (1983). Laser phase and frequency stabilization using an optical-resonator. *Applied Physics B: Photophysics and Laser Chemistry*, 31, 2, 97–105.
113. Fox, R. W., Oates, C. W., & Hollberg, L. W. (2003). Stabilizing diode lasers for high-finesse cavities. In R. D. van Zee and J. P. Looney (Eds.), *Experimental Methods in the Physical Sciences: Cavity-Enhanced Spectroscopies*, Vol. 40. Amsterdam: Elsevier Science, pp. 1–46.
114. Hamilton, M. W. (1989). An introduction to stabilized lasers. *Contemporary Physics*, 30, 1, 21–33.
115. O’Keefe, A., & Deacon, D. A. G. (1988). Cavity ring-down optical spectrometer for absorption measurements using pulsed laser sources. *Review of Scientific Instruments*, 59, 12, 2544–2551.
116. Romanini, D., & Lehmann, K. K. (1993). Ring-down cavity absorption spectroscopy of the very weak HCN overtone bands with six, seven, and eight stretching quanta. *Journal of Chemical Physics*, 99, 9, 6287–6291.
117. Hodges, J. T., Looney, J. P., & van Zee, R. D. (1996). Response of a ring-down cavity to an arbitrary excitation. *Journal of Chemical Physics*, 105, 23, 10278–10288.
118. Lehmann, K. K., & Romanini, D. (1996). The superposition principle and cavity ring-down spectroscopy. *Journal of Chemical Physics*, 105, 2, 10263–10277.
119. Hodges, J. T., Looney, J. P., & van Zee, R. D. (1996). Laser bandwidth effects in quantitative cavity ring-down spectroscopy. *Applied Optics*, 35, 21, 4112–4116.
120. Romanini, D., Kachonov, A. A., Sadeghi, N., & Stoeckel, F. (1997). CW cavity ring down spectroscopy. *Chemical Physics Letters*, 264, 316–322.
121. Ye, J., & Hall, J. L. (2000). Cavity ringdown heterodyne spectroscopy: high sensitivity with microwatt light power. *Physical Review A*, 61, 6, 061802.
122. Cossel, K. C., Adler, F., Bertness, K. A., Thorpe, M. J., Feng, J., Raynor, M. W., & Ye, J. (2010). Analysis of trace impurities in semiconductor gas via cavity-enhanced direct frequency comb spectroscopy. *Applied Physics B*, 100, 917–924.
123. Paldus, B. A., & Zare, R. N. (1999). Absorption spectroscopies: from early beginnings to cavity ring-down spectroscopy. In K. W. Busch and M. A. Busch (Eds.), *Cavity-Ringdown Spectroscopy an Ultratrace-Absorption Measurement Technique*. Washington, DC: American Chemical Society, pp. 49–70.

124. O'Keefe, A., Scherer, J. J., & Paul, J. B. (1999). Cavity-ringdown laser spectroscopy: History, development, and applications. In K. W. Busch and M. A. Busch (Eds.), *Cavity-Ringdown Spectroscopy an Ultratrace-Absorption Measurement Technique*. Washington, DC: American Chemical Society, pp. 71–92.
125. Ono, H. (2011). Moisture analysis in monosilane gas. *Pittsburgh Conference on Analytical Chemistry and Applied Spectroscopy (Pittcon)*, Atlanta, GA.
126. Funke, H. H., Raynor, M. W., Bertness, K. A., & Chen, Y. (2007). Detection of trace water vapor in high-purity phosphine using cavity ring-down spectroscopy. *Applied Spectroscopy*, 61, 4, 419–423.
127. Feng, J., Clement, R., & Raynor, M. W. (2008). Characterization of high-purity arsine and gallium arsenide epilayers grown by MOCVD. *Journal of Crystal Growth*, 310, 23, 4780–4785.
128. Yao, J., Funke, H. H., & Raynor, M. W. (2004). Measurement and control of trace moisture in corrosive gases. In *SEMI Technical Symposium (STS): Innovations in Semiconductor Manufacturing*. San Jose, CA: Semiconductor Equipment and Materials International.
129. Tiger Optics (2011). Aloha-H₂O specification sheet. Warrington, PA: Tiger Optics.
130. Tiger Optics (2011). Halo-H₂O specification sheet. Warrington, PA: Tiger Optics.
131. Tiger Optics (2011). MTO-1000-H₂O specification sheet. Warrington, PA: Tiger Optics.
132. Thorpe, M. J., Moll, K. D., Jones, R. J., Safdi, B., & Ye, J. (2006). Broadband cavity ringdown spectroscopy for sensitive and rapid molecular detection. *Science*, 311, 5767, 1595–1599.
133. Diddams, S. A., Hollberg, L., & Mbele, V. (2007). Molecular fingerprinting with the resolved modes of a femtosecond laser frequency comb. *Nature*, 445, 7128, 627–630.
134. Gohle, C., Stein, B., Schliesser, A., Udem, T., & Hänsch, T. W. (2007). Frequency comb vernier spectroscopy for broadband, high-resolution, high-sensitivity absorption and dispersion spectra. *Physical Review Letters*, 99, 26, 263902.
135. Thorpe, M. J., & Ye, J. (2008). Cavity-enhanced direct frequency comb spectroscopy. *Applied Physics B*, 91, 3–4, 397–414.
136. Adler, F., Thorpe, M. J., Cossel, K. C., & Ye, J. (2010). Cavity-enhanced direct frequency comb spectroscopy: technology and applications. *Annual Review of Analytical Chemistry*, 3, 175–205.
137. Cundiff, S. T., & Ye, J. (2003). Colloquium: femtosecond optical frequency combs. *Reviews of Modern Physics*, 75, 1, 325–342.
138. Washburn, B. R., Diddams, S. A., Newbury, N. R., Nicholson, J. W., Yan, M. F., & Jørgensen, C. G. (2004). Phase-locked, erbium-fiber-laser-based frequency comb in the near infrared. *Optics Letters*, 29, 3, 250–252.
139. Schibli, T. R., Minoshima, K., Hong, F. L., Inaba, H., Onae, A., Matsumoto, H., Hartl, I., & Fermann, M. E. (2004). Frequency metrology with a turnkey all-fiber system. *Optics Letters*, 29, 21, 2467–2469.
140. Adler, F., Moutzouris, K., Leitenstorfer, A., Schnatz, H., Lipphardt, B., Grosche, G., & Tauser F. (2004). Phase-locked two-branch erbium-doped fiber laser system for long-term precision measurements of optical frequencies. *Optics Express*, 12, 24, 5872–5880.

141. Thorpe, M. J., Balslev-Clausen, D., Kirchner, M. S., & Ye, J. (2008). Cavity-enhanced optical frequency comb spectroscopy: applications to human breath analysis. *Optics Express*, 16, 4, 2387–2397.
142. Thorpe, M. J., Adler, F., Cossel, K. C., de Miranda, M. H. G., & Ye, J. (2009). Tomography of a supersonically cooled molecular jet using cavity-enhanced direct frequency comb spectroscopy. *Chemical Physics Letters*, 468, 1, 1–8.
143. Kassı, S., Didriche, K., Lauzin, C., de Ghellinck d'Elsenghem Vaernewijckb, X., Rizopoulos, A., & Herman, M. (2010). Demonstration of cavity enhanced FTIR spectroscopy using a femtosecond laser absorption source. *Spectrochimica Acta A*, 75, 1, 142–145.
144. Foltynowicz, A., Ban, T., Masłowski, P., Adler, F., & Ye, J. (2011). Quantum-noise-limited optical frequency comb spectroscopy. *Physical Review Letters*, 107, 233002–1–5.
145. Mandon, J., Guelachvili, G., & Picqué, N. (2009). Fourier transform spectroscopy with a laser frequency comb. *Nature Photonics*, 3, 2, 99–102.
146. Adler, F., Masłowski, P., Foltynowicz, A., Cossel, K. C., Briles, T. C., Hartl, I., & Ye, J. (2010). Mid-infrared Fourier transform spectroscopy with a broadband frequency comb. *Optics Express*, 18, 21, 21861–21872.
147. Keilmann, F., Gohle, C., & Holzwarth, R. (2004). Time-domain mid-infrared frequency-comb spectrometer. *Optics Letters*, 29, 13, 1542–1544.
148. Coddington, I., Swann, W. C., & Newbury, N. R. (2008). Coherent multiheterodyne spectroscopy using stabilized optical frequency combs. *Physical Review Letters*, 100, 1, 013902.
149. Bernhardt, B., Ozawa, A., Jacquet, P., Jacquety, M., Kobayashi, Y., Udem, T., Holzwarth, R., et al. (2010). Cavity-enhanced dual-comb spectroscopy. *Natural Photonics*, 4, 1, 55–57.
150. Coddington, I., Swann, W. C., & Newbury, N. R. (2010). Coherent dual-comb spectroscopy at high signal-to-noise. *Physical Review A*, 82, 4, 043817.
151. Adler, F., Cossel, K. C., Thorpe, M. J., Hartl, I., Fermann, M. E., & Ye, J. (2009). Phase-stabilized, 1.5 W frequency comb at 2.8–4.8 μm . *Optics Letters*, 34, 9, 1330–1332.